Journal of Colloid and Interface Science 729 (2027) 141830

Contents lists available at ScienceDirect

Journal of Colloid And Interface Science

journal homepage: www.elsevier.com/locate/jcis

Droplet impact on a particle-laden liquid interface: Worthington jet dynamics and microplastic ejection from floating rafts

Muhammad Hamza Iqbal [a], Alfonso Arturo Castrejón-Pita [b], José Rafael Castrejón-Pita [a], Miguel A. Quetzeri-Santiago [c,*]

[a] Department of Mechanical Engineering, University College London, London, WC1E 7JE, United Kingdom
[b] Department of Engineering Science, University of Oxford, Oxford, OX1 3PJ, United Kingdom
[c] Instituto de Investigaciones en Materiales, Universidad Nacional Autónoma de México, Cd. Universitaria, Mexico City, 04510, Mexico

ARTICLE INFO

Keywords:
Particle-laden interfaces
Particle rafts
Droplet impact
Worthington jet
Cavity
Liquid marbles

ABSTRACT

Hypothesis: Particle-laden liquid interfaces can modify droplet-impact dynamics by altering lamella destabilisation, cavity collapse, and Worthington jet formation. We hypothesise that the size, density, and wettability of floating microparticles govern whether raindrop impact produces liquid splashing, particle ejection, or jet-mediated transport from the interface.

Experiments: We investigate millimetric water-droplet impact on quiescent pools covered by closely packed microparticle monolayers, referred to as particle rafts. Thde rafts were formed using particles with diameters of 115–780 μm, densities of 1.02–2.50 g/cm^3, and apparent contact angles of 37–157 degrees. Untreated hydrophilic or hydrophobic particles were compared with Glaco-treated superhydrophobic particles to isolate the role of wettability and immersion depth. Droplet impacts were performed under raindrop-relevant conditions, spanning $5 \lesssim We \lesssim 422$ and $6 \lesssim Fr \lesssim 479$. Orthogonal high-speed imaging and image analysis were used to quantify splashing thresholds, cavity depths, jet heights, and particle-transport pathways.

Findings: Particle rafts strongly modify canonical droplet-impact dynamics through geometric roughness, particle inertia, and capillary adhesion. Deeply immersed particles stabilise the spreading lamella and suppress particle ejection, whereas weakly immersed and superhydrophobic particles promote lamella fingering, splashing, and rapid detachment. The raft also controls cavity collapse, separating the dynamics into elastically responsive and inertially rigid regimes. Small and intermediate superhydrophobic rafts generate particle-armoured Worthington jets that fragment into liquid marbles, while larger or denser rafts suppress wave-swell formation, reduce jet height, and limit ejection. Splashing thresholds and jet heights are captured using geometric–inertial–capillary scaling, identifying when rainfall can transfer microplastics from water to air.

1. Introduction

Microplastics are now recognized as pervasive contaminants in both the hydrosphere and atmosphere alike, with substantial land-to-sea inputs and vast surface inventories documented across the global ocean [1–5]. Microplastics are commonly defined as solid synthetic polymer particles smaller than 5 mm, encompassing fragments, films, fibres and spherical particles [6,7]. Consistent definitions and size classifications have been formalized to enable cross-study comparability and reliable accounting. Beyond aquatic accumulation, airborne microplastics have been detected in remote regions and in the free troposphere, demonstrating their capacity for long-range atmospheric transport [8–10].

Microplastics have also been detected in human lung tissue and bronchoalveolar lavage fluid, underscoring plausible inhalation exposure and the need to constrain emission mechanisms at the air-water boundary [11–13]. A growing body of field evidence suggests that the ocean is not merely a sink but also a source of airborne microplastics [14]. For ocean-to-atmosphere transport to occur, plastics must first accumulate at the air-sea boundary. The sea surface microlayer (SML), a 1 – 1000 μm thick, biogeochemically enriched interface, has been shown to contain microplastic concentrations orders of magnitude higher than bulk seawater [15,16]. This concentrated reservoir forms a highly susceptible pool for emissions.

Although microplastics are currently enriched within the sea surface microlayer, reported concentrations in coastal and estuarine waters are typically found in the range of 6–90 particles L^{-1} [16–18]. Assuming these particles are confined within a 1 mm surface layer, their projected surface coverage is found in the range

* Corresponding author.
E-mail addresses: r.pita@ucl.ac.uk (J.R. Castrejón-Pita), mquetzeri@materiales.unam.mx (M.A. Quetzeri-Santiago).

https://doi.org/10.1016/j.jcis.2026.141830
Received 1 June 2026; Received in revised form 18 October 2026; Accepted 18 October 2026
Available online 26 October 2026
0021-9797/© 2026 The Author(s). Published by Elsevier Inc. This is an open access article under the CC BY license (http://creativecommons.org/licenses/by/4.0/).

of 10^{-7}–10^{-5} for the particle sizes considered here, far below the concentration considered as close packing. Natural distributions are, however, highly heterogeneous, with convergent surface slicks known to locally exceed the average concentration by two orders of magnitude [19]. We thus note that the close-packed monodisperse rafts studied here represent a controlled high-coverage limiting case rather than the current averages SML. Whether locally close-packed microplastic monolayers occur in natural surface accumulations remains unknown to the best of our knowledge, and the effects of surface coverage, polydispersity and irregular particle shape remain to be established.

The dominant, well-studied atmospheric release pathway is sea aerosol generated by breaking waves, whereby bubbles scavenge particles while rising to then expel them in surface jets upon bursting [20,21]. The microplastics are transferred via two distinct mechanisms: (i) rupture of the thin bubble cap film, which produces numerous submicron film droplets capable of carrying the smallest microplastics (typically $< 1 - 10$ μm) that become trapped within the interfacial film, and (ii) collapse of the underlying cavity, which drives a high-speed Worthington jet that breaks up into larger jet droplets capable of ejecting substantially bigger microplastics, from tens to several hundreds of micrometers, that reside at or near the bubble cap surface [21]. Laboratory measurements and global modeling suggest that this bubble-mediated emission pathway may contribute on the order of 0.1 million tonnes per year of microplastics to the atmosphere [21,22]. However, the magnitude of this bubble-mediated pathway depends strongly on wind and wave conditions. Microplastics have nevertheless been detected in coastal marine air during a sea-spray event under weak local onshore winds (< 1 m s^{-1}) [14], motivating consideration of complementary emission mechanisms.

A complementary and not well-studied emission arises from the impact of raindrops on the ocean surface. Millimetric raindrops strike the ocean surface with kinetic energies on the order of $10^{-5} - 10^{-4}$ J, driving the expansion and lift-off of an ultra-thin ($\sim 1 - 10$ μm) ejecta sheet at the neck, forming crowns that generate secondary droplets [23,24]. The onset and intensity of this splashing transition depend primarily on the impact conditions and the ensuing liquid-liquid coalescence and lamella dynamics, which determine whether the expanding sheet lifts off and fragments into airborne droplets [25]. Similarly, recent simulation-experiment studies have demonstrated that secondary droplets produced by rainfall impact can directly entrain small-sized (6 μm) particles from the ocean surface. In fact, the particle concentration in the ejecta remains comparable to that in the surface water layer [26]. Upscaling these single-impact dynamics with global rainfall statistics suggests that this mechanism may release up to $\sim 10^{14}$ microplastic particles into the atmosphere annually [26]. Earlier aerosol studies further have shown that prompt splash on aqueous solution generates a population of micron-sized secondary droplets that can eject solid residues (up to 30 μm) into the air, with the quantity of this airborne material increasing with impact inertia [27,28].

A central feature of droplet impact on a liquid pool is the emergence of a Worthington jet formed when the transient cavity created by the impacting drop collapses and focuses momentum upward along the symmetry axis [29]. This vertical jet can accelerate fluid parcels to several meters per second [30], projecting droplets to heights far exceeding those generated by crown splash alone. Thus, representing an efficient upward transport pathway for any material residing at or near the interface, including microplastics concentrated within the sea surface microlayer, into the air/atmosphere. The height, morphology, and breakup of the jet are governed by a complex interplay of inertial, capillary and gravitational forces, which define distinct jetting regimes. These force balances are captured by the Weber number, $We = \rho U^2 D/\sigma$, which compares inertial to capillary stresses, and the Froude number, $Fr = U^2/gD$, which compares inertial to gravitational forces, where ρ, U, D, σ and g denote liquid density, impact velocity, droplet diameter, surface tension and gravitational acceleration, respectively.

Numerical and experimental studies of drop-pool impact dynamics have shown that, as the Weber and Froude numbers increase, the collapsing cavity transitions systematically through U-shaped, V-shaped, and W-shaped profiles, each producing a distinct jet type, from short thick jets to high-speed slender jets and long thick jets, respectively, with correspondingly different pinch-off behaviors [30,31]. These transitions arise from two underlying jetting pathways, namely a thin, rapidly rising “singular jet” driven by the focused collapse of a capillary wave at intermediate We/Fr and a slower, thicker “cavity jet” produced by the large-scale retraction of the crater at higher We/Fr [31]. Furthermore, increasing impact velocity leads to a well-defined regime progression, where the ejected secondary droplet can not only be comparable to, but even exceed, the size of the original impacting drop, underscoring the capacity of this mechanism to expel substantial volumes of surface water [32]. Whether the jet fragments into airborne droplets is governed by the critical balance between viscous and capillary-inertial stresses, captured by the Ohnesorge number $Oh = \mu/\sqrt{\rho\sigma D}$, where μ denote liquid viscosity. Above a threshold Ohnesorge number ($Oh \approx 0.09$), viscous damping suppresses Rayleigh-Plateau jet breakup entirely, even at high impact velocities [33]. These dynamics are sensitive to surface topology; impacts on pre-existing wave troughs, for instance, can triple the jet height and increase the total ejected liquid volume by over sixfold compared to a flat surface, enhancing aerosolisation [34].

In addition, the splashing and jet dynamics are altered when the free surface is no longer a bare (clean) liquid but is covered by a closely packed monolayer: a “particle raft.” Related droplet-impact studies on particulate substrates have shown that mobile particles can strongly modify both splashing and particle transport. On solid substrates coated with a loose particle monolayer, particle accumulation and jamming ahead of the spreading rim can trigger corona splashing [35], while impact onto bulk granular media produces distinct spreading and splashing regimes together with particle ejection [36]. Floating particle rafts differ from these configurations because the particles reside directly at the deformable liquid–air interface and therefore participate in cavity formation, collapse, and subsequent jet dynamics.

Particles residing at the liquid–air interface deform the surrounding meniscus through a balance between gravity and surface tension. At the particle scale, this balance is characterized by the particle Bond number $Bo_p = (R_p/\ell_c)^2 = (\rho - \rho_a)gR_p^2/\sigma$, [37]. Where R_p is the particle radius and ℓ_c is the capillary length. For $Bo_p \ll 1$, capillary effects dominate hydrostatic deformation, and even small interfacial slopes can generate long-ranged capillary interactions that drive particle migration and clustering. These interactions, classically described in studies of capillary attraction between floating bodies [38,39], and in the broader framework of interfacial colloidal assembly [40], cause particles with similar meniscus curvature to attract while those with opposite curvature repel, leading to the Cheerios effect [41]. Once trapped at the interface, particles experience attachment energy arising from the replacement of a patch of fluid-fluid interface by particle-fluid interfaces and form mechanically stable monolayers whose structural and elastic properties have been widely characterized [42,43]. When monodisperse particles with uniform wettability accumulate at an interface, capillary forces draw them into contact and favor dense hexagonal packing that minimizes interfacial energy, producing a mechanically coherent, quasi-solid raft [44,45]. Close-packed particle rafts have been shown to behave collectively as two-dimensional elastic solids, supporting anisotropic stresses and strains and exhibiting buckling under compression and fracture under tension [46]. Their response is not purely elastic, however, as stress transmission within compressed rafts also exhibits a granular character [47]. Particle rafts therefore combine continuum-scale elastic behavior with particle-scale rearrangement and granular stress transmission.

In addition, their load-bearing response under transverse indentation and their wrinkling and force response under planar compression have been characterized experimentally and theoretically [48,49]. These studies establish that particle rafts can sustain and redistribute externally imposed loads through collective particle–interface mechanics.

The response under impulsive droplet loading remains comparatively less explored. Unlike quasi-static indentation or in-plane compression, droplet impact simultaneously drives rapid lamella expansion, transient cavity formation and collapse, and subsequent Worthington-jet formation.

Here, we investigate droplet impact dynamics onto quiescent pools covered with monodisperse particle rafts. In each experiment, a single particle type (defined by one size, density, and wettability) is used to form a uniform monolayer raft, enabling systematic variation of interfacial properties across fluorescent polyethylene, polyethylene (FPE and PE) and glass in both untreated and Glaco-treated superhydrophobic states. Orthogonal high-speed imaging resolves the spatiotemporal evolution of the ejecta sheet, cavity and the Worthington jet, allowing us to quantify jet height, breakup pathways and the conditions governing microplastic ejection from the interface. Together, these measurements provide the first direct characterization of the role of particle rafts on the dynamics of drop-pool impact and, consequently, the mechanisms governing atmospheric release of microplastics from the ocean surface.

2. Experimental details

2.1. Materials

Deionized water was obtained from a Milli-Q purification system (Millipore, resistivity 18.2 MΩ · cm). Its physical properties at 22 ± 1 °C were a density of 998 kg m^{-3}, dynamic viscosity of 1.0 mPa s, and surface tension of 72.8 mN m^{-1}.

The experiments utilized spherical microparticles of various materials, sizes, and densities to form the floating rafts. Polyethylene microspheres (Cospheric LLC, USA) were used in two density grades: fluorescent green polyethylene (FPE) ($\rho_P = 1.02$ g cm^{-3}) with mean diameters of 115, 231, 327, 550 and 780 μm; and white polyethylene (PE) ($\rho_P = 1.35$ g cm^{-3}) with mean diameters of 327 and 780 μm. Hydrophilic glass microspheres (Glass) ($\rho_P = 2.50$ g cm^{-3}, $D_P = 625$ μm) were sourced from Thermo Fisher Scientific. The PE and FPE spheres were used as controlled model microplastics, whereas the glass spheres served as the sole non-plastic reference system for examining the effects of increased particle density and contrasting wettability. For all particle types, the reported diameters correspond to the mean values of the supplier's nominal size distributions. The glass particles had a broader nominal diameter range of 500–750 μm, represented here by $D_p = 625$ μm, whereas the PE and FPE particles were supplied in narrow size fractions. The glass rafts therefore exhibit greater local polydispersity and less perfectly ordered packing than the PE and FPE rafts.

All particles were used as received, without any initial surface modification. Selected batches of each particle type were rendered superhydrophobic by coating their surfaces with Ultra Ever Dry Glaco (Soft99 Co., Japan) to investigate the influence of surface wettability on the impact dynamics. The Glaco-treated (G-FPE, G-PE, and G-Glass) particles were left to dry under ambient laboratory conditions for 24 h, producing a thin layer of hydrophobic nanoparticles that imparted a superhydrophobic finish. Previous AFM characterization of Glaco treatment on glass has reported a surface-feature height of approximately 0.8 μm [50], i.e. over two orders of magnitude smaller than the particle

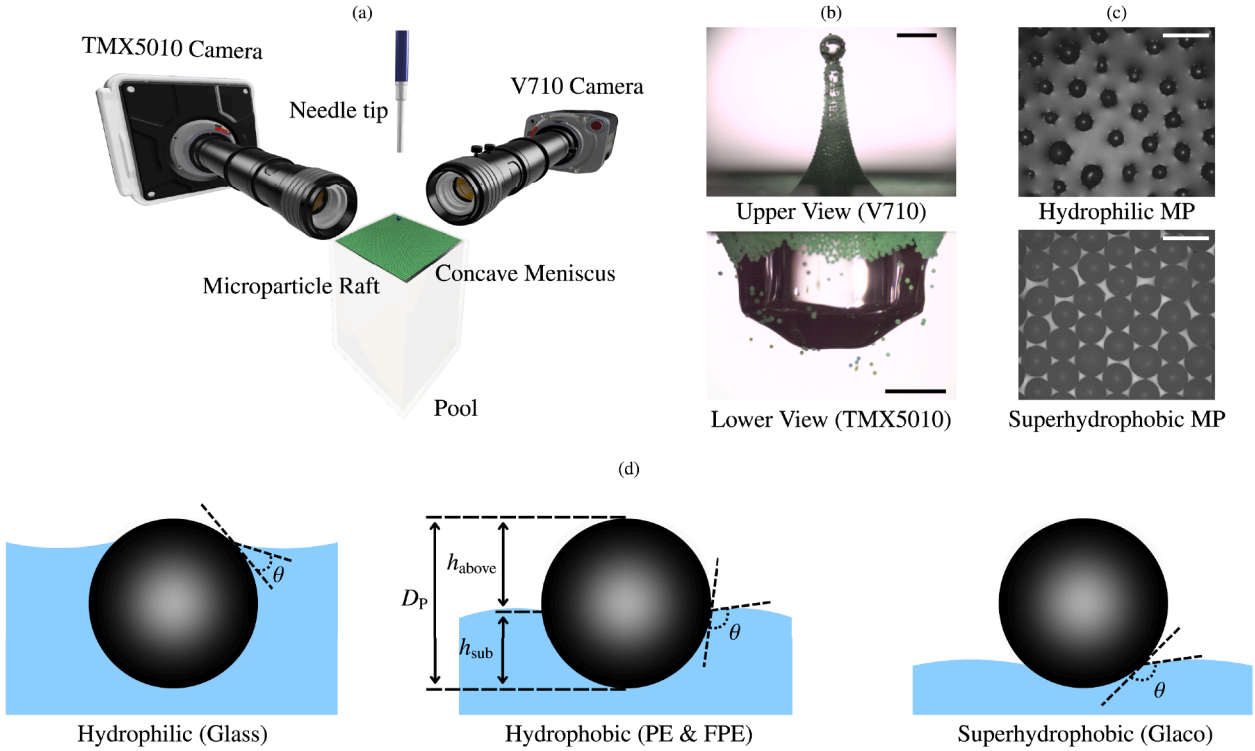


Fig. 1. Experimental configuration and characterization of floating microparticle rafts. a) Sketch of the droplet-raft impact apparatus. Millimetric water droplets are generated from a syringe pump and needle and released onto a quiescent pool whose surface is coated with a closely packed particle raft. A high-speed side-view imaging system records the droplet impact, crater formation and Worthington jet dynamics. b) Representative top-view (top) and side-view (bottom) images from the high-speed cameras showing the hexagonally packed monolayer of 780 μm FPE microparticles and the corresponding interfacial profile at the particle scale. Scale bars are 2 mm. c) Optical-profilometer scans of hydrophilic 625 μm glass spheres (top) and Glaco-treated 550 μm FPE spheres (bottom), providing direct measurements of the emerged height, h_{above}, relative to the undisturbed interface. For the untreated glass particles, the apparent uneven spacing is the result of both their broader nominal size distribution (500–750 μm) and their large immersion depth, i.e. only small emerged particle caps are visible and it does not imply an incomplete interfacial coverage. Scale bars are 1 mm. d) Schematic immersion geometries for hydrophilic, hydrophobic and superhydrophobic microparticle spheres. The submerged depth (h_{sub}), emerged height (h_{above}), and the apparent contact angle (θ) are indicated (see Table 1), corresponding to the geometric relation used to compute wettability at negligible Bond number. Not to scale.

diameters used here. No measurable surface-tension change of the water pool was observed after exposure to Glaco-treated particles (72.4 ± 0.5 to 72.2 ± 0.5 mN m^{-1}), and the particles remained strongly emerged with no progressive wetting. Interparticle friction variations caused by the Glaco coatings were not assessed in this work and are assumed negligible.

2.2. Method

2.2.1. Overview of the experiments

The experimental apparatus was designed for the optimum visualization of the interplay between a falling droplet under gravity and a floating particle raft on a water pool (Fig. 1a). Droplets were generated using an AL-300 Aladdin InfusionONE syringe pump operated at a constant flow rate of 20 μL min^{-1}. A blunt-end stainless-steel dispensing needle (Gauge 20, inner diameter, 0.61 mm) was used to form pendant droplets of deionized water, which were detached under their own weight to produce droplets of diameter $D = 2.55$ mm. The impact velocity, U, was systematically varied between 0.39 and 3.46 m s^{-1} by adjusting the height of the dispensing needle using a precision mechanical vertical stage. Each impact condition was repeated at least three times, while conditions close to the splash/no-splash transition were repeated four to five times. Splashing was defined by the complete detachment of at least one secondary droplet from the ejecta sheet, or the crown. The critical Weber number was taken as the lowest tested Weber number at which the onset of splashing is observed and confirmed through the repeated experiments. Across the explored impact velocities, the Reynolds and capillary numbers span approximately $9.9 \times 10^2 \lesssim Re \lesssim 8.8 \times 10^3$ and $5.4 \times 10^{-3} \lesssim Ca \lesssim 4.8 \times 10^{-2}$, respectively, while the Ohnesorge number is $Oh \simeq 2.3 \times 10^{-3}$. The experiments therefore lie in a high-Re, low-Ca, low-Oh regime in which bulk-liquid viscous stresses are relatively small compared with inertial and capillary stresses during the early impact dynamics.

A rectangular acrylic tank (internal dimensions: $65 \times 49 \times 85$ mm) was used as the impact pool. A concave meniscus was generated by leaving a small clearance below the rim when filling the tank with deionized water. This configuration produced a stable inward-sloping free surface that promoted migration and confinement of the particle raft towards the center. A depth to droplet diameter ratio of $H/D \approx 33$ ensures negligible bottom effects, and the pool can therefore be considered semi-infinite. The minimum lateral distance from the impact center to the nearest sidewall was $L_w/D \approx 10$–13, where L_w denotes the center-to-wall distance. This confinement ratio is likewise sufficiently large to minimize early-time wall reflections, as surface wave propagation from the impact site to the walls occurs on a timescale much longer than that of cavity collapse and Worthington jet formation.

Two synchronized high-speed cameras were used to resolve the droplet impact dynamics from vertically offset side views centered on the impact plane (Fig. 1b). A Phantom V710 high-speed camera (1280 × 800 pixels) equipped with a Navitar 12× lens recorded the upper region at 7500 fps with an exposure time of 60 μs, resolving the splashing, particle ejection, and the formation of the subsequent Worthington jet. Simultaneously, a Phantom TMX high-speed camera (1280 × 800 pixels) fitted with the same lens recorded the lower region at 7500 fps with an exposure time of 20 μs, resolving crater formation within the particle raft and subsequent cavity collapse. Both views were illuminated using a Photofluor II lamp (89 North), providing diffuse front lighting. The imaging resolutions were approximately 55 pixels mm^{-1} (18 μm pixels^{-1}) and 86 pixels mm^{-1} (12 μm pixels^{-1}) for the upper and lower views, respectively. Based on a three-pixel criterion, the corresponding practical minimum particle size detection limits are approximately 55 and 35 μm. Features, including aerosol-sized droplets, below these limits were therefore not resolved. The spatial resolutions were 55 and 86 pixels mm^{-1}, for the upper and lower views, respectively.

All experiments were performed under standard ambient laboratory conditions at a temperature of $22 \pm 1\,°C$ and a relative humidity of 45 – 55%.

2.2.2. Particle positioning

The microplastic particles were gently deposited onto the water surface by lightly tapping the storage container to release a controlled amount of particles. A rubber suction bulb was then used to blow gentle air streams across the surface, enabling fine adjustment of particle positions and preventing overlap, particularly for the smaller particles that tended to cluster. To achieve a closely packed monolayer, the tank walls were lightly tapped to generate surface waves that promoted self-assembly into a uniform two-dimensional hexagonal packing. This procedure was repeated until a continuous and tightly packed particle raft was formed. Following each droplet impact, additional particles were introduced to restore full surface coverage, and the arrangement was fine-tuned using the same procedure. Real-time feedback from the high-speed cameras was used to verify the uniformity and ensure that each droplet impacted the center of a fully packed raft, maintaining consistency and reproducibility across all experiments.

2.2.3. Profilometer

The wettability of each microparticle type was characterized from its equilibrium immersion geometry at the air–water interface. Particles were gently deposited onto a quiescent water surface, and their emerged height, h_{above}, relative to the undisturbed far-field interface was measured using a vertical-scanning optical profilometer (InfiniteFocus, Alicona GmbH; Fig. 1c). The submerged depth was calculated as $h_{\text{sub}} = D_p - h_{\text{above}}$, and the dimensionless immersion ratio was defined as $h = h_{\text{sub}}/D_p$ (Fig. 1d).

The particle-scale Bond number was defined as $Bo_p = (R_p/\ell_c)^2$, where $R_p = D_p/2$ and $\ell_c = 2.7$ mm. Across the particle sizes used, $4.5 \times 10^{-4} \leq Bo_p \leq 2.1 \times 10^{-2}$, confirming both a low-Bond-number regime and a locally flat-interface approximation at the particle scale. For a spherical particle intersecting a locally flat interface, the apparent geometric contact angle measured through the aqueous phase is given by $\theta = \cos^{-1}(2h - 1)$. Here, θ denotes the apparent geometric contact angle inferred from the measured equilibrium immersion depth. It should not be interpreted as an independently measured microscopic Young, advancing, or receding contact angle, since local meniscus curvature,

Table 1
Physical properties of microparticles.

Microparticle	D_p μm	ρ_p g/cm^3	h h_{sub}/D_p	θ degrees	B nN m
FPE (untreated)	115, 231, 327, 550, 780	1.02	0.41 ± 0.03	100 ± 5	0.47, 1.90, 3.80, 10.76, 21.64
G-FPE (treated)	115, 231, 327, 550, 780	1.02	0.04 ± 0.02	157 ± 3	0.12, 0.50, 1.00, 2.84, 5.70
PE (untreated)	327, 780	1.35	0.43 ± 0.02	98 ± 4	3.81, 21.69
G-PE (treated)	327	1.35	0.06 ± 0.03	152 ± 4	1.40
Glass (untreated)	625	2.50	0.90 ± 0.03	37 ± 4	7.79
G-Glass (treated)	625	2.50	0.11 ± 0.04	141 ± 6	8.36

D_p is the particle diameter, ρ_p is the particle density, h is the dimensionless immersion ratio, θ denotes the apparent geometric contact angle calculated from h (see Experimental section), and B is the estimated capillary bending stiffness. Values are reported as mean ± standard deviation.

contact-line pinning and surface heterogeneity may introduce additional uncertainty.

The equilibrium immersion depth is governed by a balance of particle weight, buoyancy and capillary forces and therefore depends on the particle size, density, wettability, the liquid surface tension and other contact-line conditions. While a vertical force balance can describe this equilibrium, it cannot independently predict h_{sub} without specifying the contact angle and meniscus geometry. Consequently, we restrict our study to reporting the immersion depth from experimental measurements, i.e. we report the mean ± the standard deviation for each material and treatment.

3. Results and discussions

In our experiments, we studied the effect of particle size and wettability on the resulting dynamics following droplet impact on rafts. Fig. 1 illustrates the experimental setup (a), shows an example of the impact dynamics (b), the typical raft geometries prior impact (c), and defines the experimental parameters (d). In brief, a 2.55 mm water droplet is generated from a syringe pump and released onto a quiescent pool whose surface is covered with a close-packed monolayer of monodisperse microparticles (Fig. 1a). Orthogonal high-speed imaging captures the resulting crater/cavity formation, the cavity collapse and the resulting Worthington-jet dynamics (Fig. 1b). The droplet-raft impact experiments are dependent on the interfacial mechanics of the microparticles within the floating monolayer raft.

Prior to the impact, the microparticles were assembled into a uniform hexagonal raft, and the equilibrium immersion geometries were measured directly using vertical-scanning optical profilometry (Fig. 1c and Section 2.2.3). The corresponding apparent geometric contact angle was calculated from $\theta = \cos^{-1}(2h - 1)$. Glaco treatment markedly reduced the immersion ratio, from 0.41 to 0.04 for FPE, from 0.43 to 0.06 for PE, and from 0.90 to 0.11 for glass (Table 1), demonstrating the strong influence of wettability on the equilibrium particle position at the interface.

3.1. Splashing dynamics

As expected, splashing is influenced by both the raft characteristics and the impact properties. The influence of the raft surface coverage on splashing is first quantified by mapping impact outcomes across the Weber number and particle size (Fig. 2a-b). For example, on a clean water (raft-free) surface,(crown) splash first occurs at $We \approx 193$, this in agreement with previous studies [27]. Under these conditions, the expanding lamella lifts off to form a well-defined crown that subsequently fragments into secondary droplets (splashing). In this regime, splashing is predominantly pool-driven, with the ejecta originating from the pool. In contrast, impacting a fully packed microparticle raft (as seen in Fig. 1c), fundamentally alters both the splashing threshold and the resulting dynamics. Unlike clean water, splashing on particle-coated interfaces becomes particle-size dependent, where the ejecta volume can proceed from the pool or the impacting droplet (Fig. 2c-d). For the smallest particles used here, i.e., 115 μm of untreated FPE (Fig. 2a), splashing is hindered, with the onset occurring at $We \approx 251$. This suggests that a densely packed monolayer of small particles stabilizes the pool lamella and suppresses the growth of rim perturbations. In fact, when splashing does occur, it is predominantly prompt splashing, characterized by the ejection of ~ 10 secondary microdroplets from the droplet rather than from the pool; a reduced crown height is also observed (Fig. 2c).

Intermediate FPE particle sizes (231 and 327 μm) exhibit prompt splashing at lower Weber numbers than clean water ($We \approx 163$), and increase the number of secondary microdroplets. As particle size increases across this range, prompt splashing becomes progressively more violent (i.e., more secondary droplets are generated) and the crown height is further diminished. For the largest untreated FPE particles (550 – 780 μm), splashing is triggered at even lower Weber numbers ($We \approx 101$) and is characterized by a pronounced fingering of the crown lamella, which subsequently breaks up into secondary droplets (Fig. 2c). Although the interface is not a rigid solid, a monolayer raft acts as a rough substrate, with its roughness controlled by the particle size. Under these conditions, a raft with particle diameter $D_p \gtrsim 550$ μm presents larger heterogeneity (and roughness) than a $D_p \lesssim 327$ μm raft. As with rough surfaces, large-amplitude roughness trigger rim perturbations that promote fingering and breakup [51]. In contrast, smaller particles act as a quasi-continuous coating that damps interfacial deformation.

In fact, the splashing behavior is not solely governed by particle size; both particle density and wettability determine the immersion depth and the contact angle which in turn control raft inertia and the lamella lift-off. For instance, untreated PE spheres ($\rho_P = 1.35\,g\,cm^{-3}$) at 327 and 780 μm consistently splash at lower Weber numbers than their lower-density FPE counterparts ($\rho_P = 1.02\,g\,cm^{-3}$). Conversely, hydrophilic glass spheres ($\rho_P = 2.50\,g\,cm^{-3}$, 625 μm) are substantially more submerged ($h \approx 0.90$) and exhibit a small geometric contact angle ($\theta \approx 37°$), such that only a limited fraction of the particle protrudes above the interface. As a result, splashing occurs only at significantly higher Weber numbers ($We \approx 160$), counter to expectations based on particle size and density alone. This demonstrates that the immersion depth plays a dominant role, alongside particle size and density, in setting the splashing threshold.

In contrast, Glaco-treated (superhydrophobic) particles exhibit a systematic and monotonic dependence of the splashing threshold on particle size (Fig. 2b). Their shallow immersion depths ($h < 0.11$) and large apparent contact angles ($\theta > 141°$) effectively eliminate the wettability heterogeneities present in the untreated rafts, yielding a chemically homogeneous interface. As a result, particle size emerges as a primary parameter governing splashing.

The splashing threshold for small Glaco-treated particles, i.e., 115 – 327 μm, is markedly reduced compared to untreated particles, decreasing from $We \approx 251 - 163$ to $We \approx 101 - 65$. This behavior is also seen for large untreated and treated PE/FPE particles, i.e., 550 – 780 μm, where the splashing threshold moves from $We \approx 101$ to $We \approx 65$. Notably, glass particles (625 μm), also follow this monotonic trend, with the threshold reduced from $We \approx 160$ to $We \approx 65$. This behavior reflects the combined effects of reduced immersion depth and enhanced effective roughness, as Glaco-treated particles sit high at the interface and produce pronounced geometric heterogeneities. The observed splashing behavior is consistent with a large advancing dynamic contact angle of the spreading droplet, which promotes lamella lift-off and early breakup on superhydrophobic Glaco-treated solid surfaces [52]. Consistent with this past work, Glaco-treated rough solid surfaces exhibit similarly reduced splashing thresholds ($We \approx 79$), reinforcing the role of the contact angle and interfacial roughness in facilitating splashing [51]. As in the untreated case, the violence of the splash on superhydrophobic rafts increases with particle size, with larger particles producing more pronounced fingering and secondary droplet formation (Fig. 2d).

Aiming to scale these observations, we proposed a parameter Λ_n that includes the three dominant parameters governing the impact dynamics, i.e. a scale/size ratio, a density ratio, and wettability. The particle-size to droplet diameter ratio D_p/D sets the characteristic roughness scale encountered by the spreading lamella, while the density ratio ρ_p/ρ represents the relative particle inertia and resistance to the lamella inertia. The final contribution represents the equilibrium particle protrusion at the interface. For the measured immersion geometry, $\cos\theta = 2h - 1$, and therefore $1 - \cos\theta = 2(1 - h) = 2h_{above}/D_p$. Here, θ is the apparent geometric angle inferred from the measured equilibrium immersion depth. Thus, $1 - \cos\theta$ is equivalently a direct measure of the fraction of the particle protruding above the undisturbed interface. Wettability, contact-line pinning, and hysteresis can influence this equilibrium position; their net effect on the initial raft geometry is therefore contained in the experimentally measured immersion depth. Dynamic contact-angle hysteresis during impact is not independently measured in the present experiments.

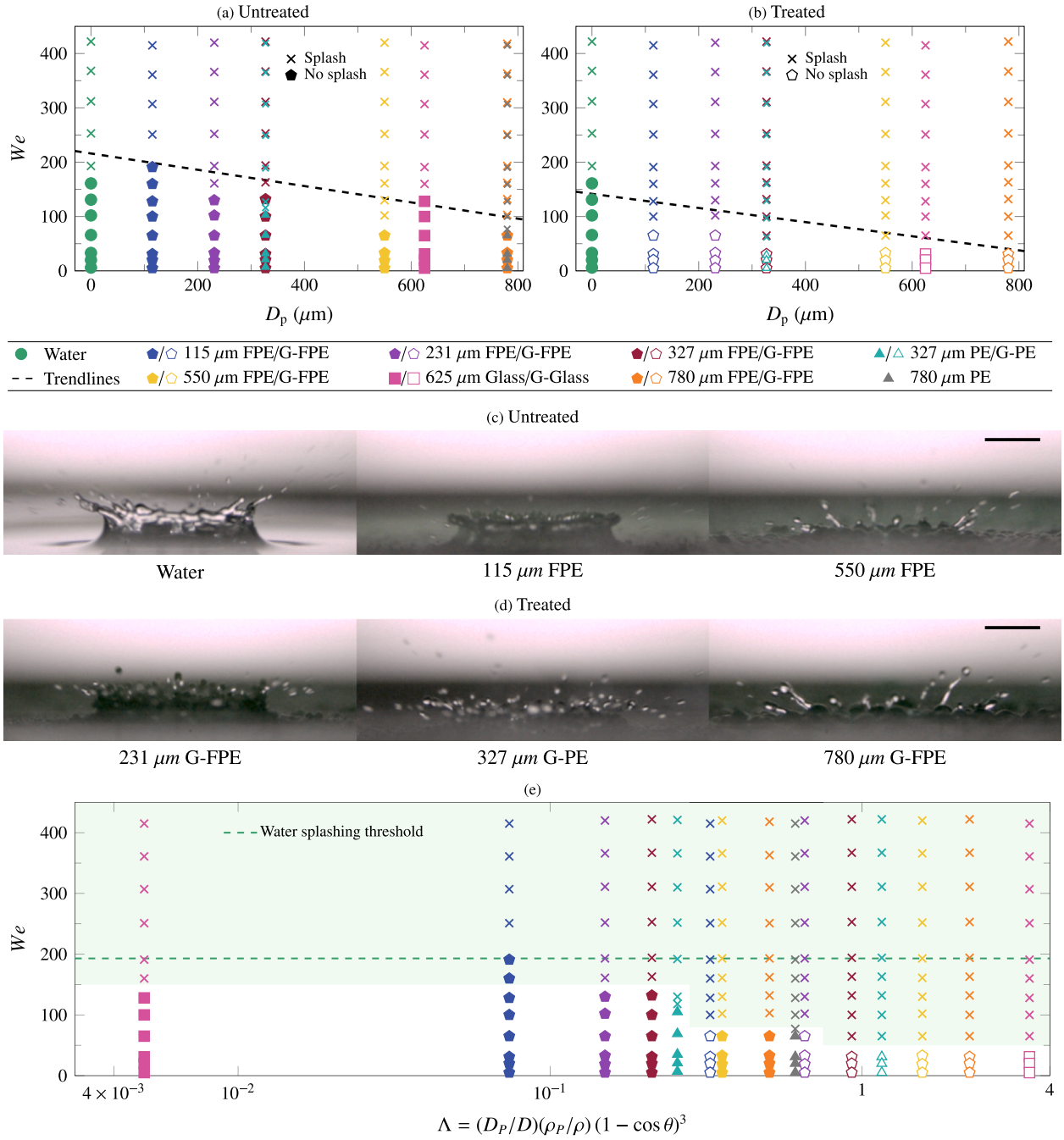


Fig. 2. Splashing dynamics on particle rafts. a,b) Impact outcomes mapped in the (We, D_p) plane for (a) clean water + untreated and (b) Glaco-treated (superhydrophobic) particle rafts, showing the transition from spreading to splashing across particle diameters and Weber numbers. The critical Weber number corresponds to the lowest tested impact condition at which splashing is observed. The dashed lines show the empirical trend of the splashing threshold, highlighting the progressive decrease in the critical Weber number as particle diameter increases. The Glaco treatment (superhydrophobic) produces a shallow particle immersion and large apparent contact angles that shift the splashing threshold to low Weber numbers. c,d) Side-view snapshots of droplet impact at $t = 0.05$ ms, after impact at $We = 346 \pm 3$, comparing splashing morphologies on untreated (c) and Glaco-treated (d) particle rafts. For both, the splashing morphology evolves from classical crown splashing on water to prompt splashing for small particles (115 – 327 μm), before reverting to crown-like splashing for larger particles (550 and 780 μm). e) Our scaling, Λ, collapse of all experiments in the (We, Λ) plane. The green dashed line indicates the splashing threshold on clean water for reference. Scale bars are 2 mm. (For interpretation of the references to color in this figure legend, the reader is referred to the web version of this article.)

Under these conditions, we consider a general scaling of the form $\Lambda_n = (D_p/D)(\rho_p/\rho)(1-\cos\theta)^n$. Integer exponents $n = 1$–4 were examined with $n = 3$ producing the clearest distinction between splash and no-splash events across the complete dataset. The exponent is therefore semi-empirical and is not presented as a first-principles prediction. The resulting scaling parameter is

$$\Lambda = \left(\frac{D_p}{D}\right)\left(\frac{\rho_p}{\rho}\right)(1-\cos\theta)^3 \tag{1}$$

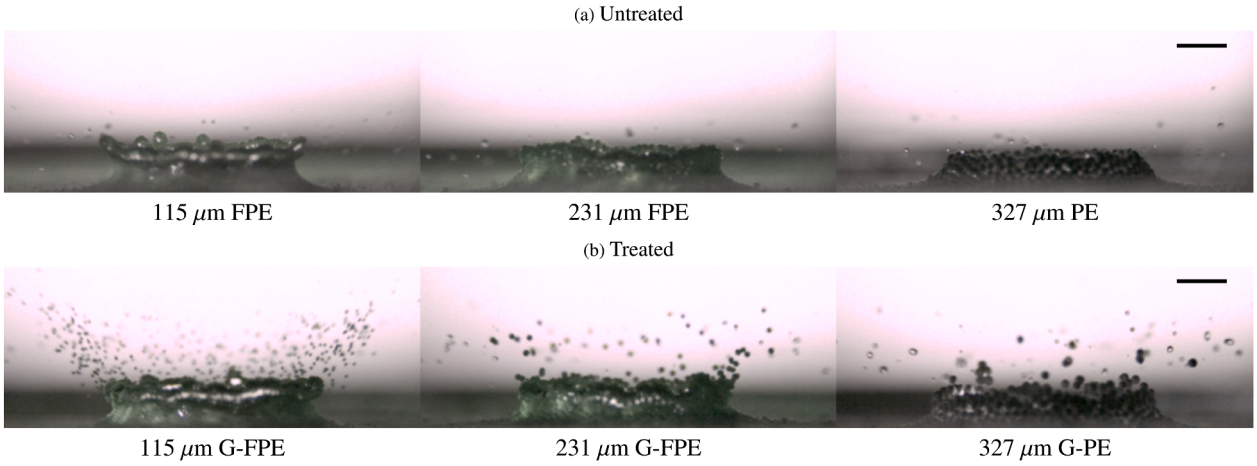


Fig. 3. Impact-driven particle ejection during droplet splashing on FPE/PE rafts at $We \approx 415$**.** a,b) Side-view snapshots at $t = 2.8$ ms after impact comparing particle splash for untreated (a) and Glaco-treated (b), illustrating the strong contrast between suppressed splash for hydrophobic particles and prolific radial ejection for superhydrophobic particles. For untreated rafts, only limited particle detachment is observed, whereas treated rafts exhibit widespread scattering due to minimal interfacial pinning. Scale bars are 2 mm.

Fig. 2e shows the experimental results in the (We, Λ) space. Across the different particle materials, sizes and surface treatments, the data collapse into broadly two separated regions, i.e. splashing and non-splashing.

At sufficiently small Λ, corresponding to small and weakly protruding particles, the raft introduces only a weak perturbation and splashing remains primarily governed by the underlying liquid-pool dynamics. The critical Weber number therefore approaches the clean-water threshold. As Λ increases, rafts with $\Lambda \gtrsim 0.5$, corresponding to larger particles, greater particle inertia or more strongly protruding hydrophobic particles, increasingly destabilize the spreading lamella and promote splashing at lower Weber numbers.

The principal exception is the untreated 115 μm FPE raft, for which splashing is delayed to $We \approx 251$. The small, densely packed particles form a quasi-continuous, membrane-like layer that damps rim perturbations and increases the resistance of the lamella to breakup, an effect not explicitly represented by Λ. Apart from this identifiable low-Λ exception, the scaling captures the general shift towards lower splashing thresholds for increasing particle size, density and protrusion. The collapse therefore demonstrates that splashing on particle rafts is governed by a combined geometric–inertial–capillary response rather than by a single particle characteristic.

3.2. Impact-driven particle ejection during splashing

Beyond controlling the splashing threshold and behavior, wettability also governs whether splashing is accompanied by particle ejection at the moment of impact. Particle ejection occurs during the early stages of droplet-raft interaction, as horizontal momentum from the impacting droplet is transferred to the particle monolayer during the lamella expansion and cavity formation. For untreated particle rafts, impact-driven particle ejection is strongly suppressed across the entire parameter space explored. Small untreated particles (115 – 231 μm) exhibit only limited ejection, and only at the highest impact speeds ($We \gtrsim 277$), typically expelling fewer than 5-10 particles (Fig. 3a). Their substantial immersion depths ($h \approx 0.4 - 0.9$) result in strong capillary adhesion to the interface [42], such that significant impulse is required to detach particles from the raft. For larger untreated particles (≥ 327 μm), impact-driven particle splash is never observed. In this regime, increased particle inertia and larger interfacial contact areas further inhibit displacement, and splashing proceeds almost exclusively through liquid fragmentation, with particles remaining bound to the interface.

In stark contrast, Glaco-treated superhydrophobic particles exhibit enhanced impact-driven particle ejection. For small treated particles (115 – 327 μm), particle splash initiates at low Weber numbers ($We \approx 65$) and intensifies rapidly with impact energy, ejecting tens to hundreds of particles radially from the impact site (Fig. 3b). Their extremely shallow immersion depths ($h \approx 0.04 - 0.11$) render the particles quasi-buoyant, resting on the interface with minimal capillary pinning [42,43]. As a result, the horizontal impulse associated with lamella expansion readily overcomes weak inter-particle cohesion, leading to rapid rupture and dispersal of the raft.

For larger Glaco-treated particles (550 – 780 μm), impact-driven particle ejection is only observed at the highest Weber numbers. At lower impact inertia, splashing remains predominantly liquid-dominated, with particles remaining bound to the interface despite vigorous lamella breakup. This transition reflects the increased impulse required to accelerate the larger particle mass. The suppression of impact-driven ejection is most pronounced for glass spheres, which are never observed to eject during splashing, irrespective of surface treatment. Their high density ($\rho_P \approx 2.50$ g cm^{-3}) makes particle inertia dominant, pinning them to the interface during impact and preventing detachment even under superhydrophobic conditions.

Together, these observations demonstrate that impact-driven particle ejection during splashing is governed by a competition between capillary adhesion and particle inertia. While superhydrophobic treatment removes wettability-induced pinning and promotes particle mobility, particle size and density ultimately determine whether splashing transitions from a purely liquid-dominated process to one accompanied by direct particle entrainment.

3.3. Jet dynamics

Our results indicate that raft particles modify the dynamics of the cavity depth and collapse in Worthington jets. Here, based in our observations, we propose a scaling law for the Worthington jet height and particle entrainment. In our analysis, the maximum dimensionless Worthington jet height, H_J/D, is measured as a function of the Froude number (Fig. 4a-b). Following prior work, the maximum vertical distance from the undisturbed pool surface to the tip of the central liquid column was defined as the jet height, H_J. Events with $H_J/D > 0.5$ were classified as fully developed Worthington jets, while smaller axial protrusions were classified as surface rebounds. In our experiments, on a clean water surface, the onset for Worthington

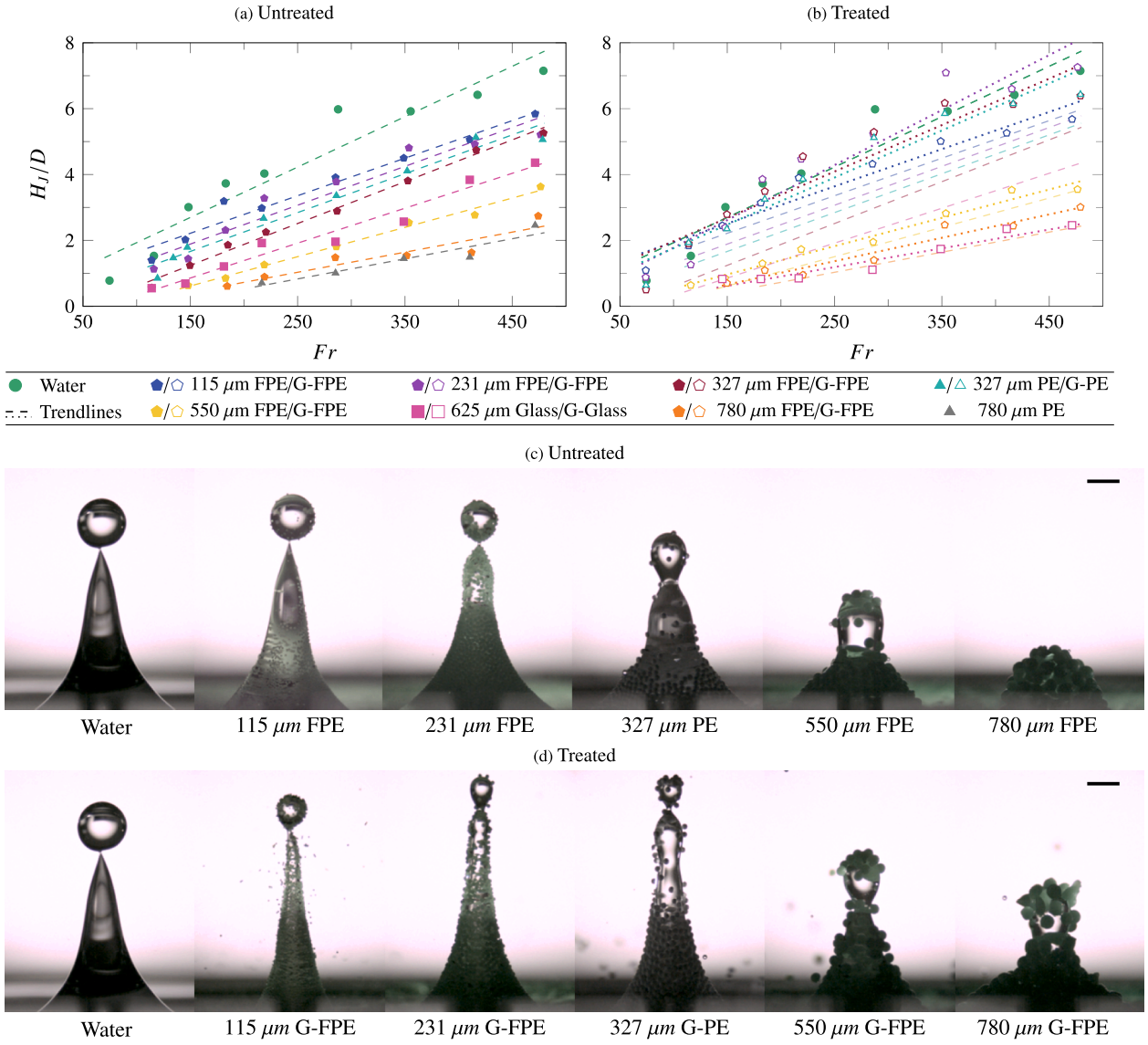


Fig. 4. Influence of the particle raft size on the Worthington jet height. Solid symbols represent untreated particles, while hollow symbols represent Glaco-treated particles; dashed and dotted lines added to guide the eye. a,b) Maximum dimensionless jet height, H_J/D, as a function of the Froude number for clean water and particle rafts of varying diameter; (a) shows results for untreated particles and (b) shows Glaco-treated particles. For untreated rafts, the onset of jetting shifts systematically to higher Fr with increasing particle size with the maximum jet height decreasing monotonically. In contrast, Glaco-treated rafts exhibit earlier jet formation and a non-monotonic dependence of jet height on particle diameter, with the tallest jets observed for intermediate sizes (231 and 327 μm). Data points represent mean values from repeated experiments; the associated standard deviations are smaller than the symbols and are therefore not shown. In panel (b), dashed lines for untreated rafts are shown for reference. c,d) Side-view snapshots of the Worthington jet at the instant of maximum height at $Fr = 417 \pm 3$, comparing untreated (c) and Glaco-treated (d) particle rafts with clean water. Scale bars are 2 mm.

jet formation is found at $Fr \gtrsim 70$, which is consistent with earlier works [31].

Results indicate that untreated particle rafts delay and suppress jet formation, as seen in Fig. 4a. For untreated PE and FPE rafts, the onset of jet formation systematically shifts to higher Fr numbers with increasing particle size. For example, jets appear for $Fr \gtrsim 110$ for particle diameters of 115, 231, and 327 μm, while larger particles require substantially faster impacts, with thresholds of $Fr \gtrsim 148$ for 550 μm and $Fr \gtrsim 184$ for 780 μm. Beyond the onset, the maximum jet height decreases monotonically with particle size, indicating that large particles impede the upward focusing of momentum required for cavity collapse (Fig. 4c). In fact, changing particle density, at fixed size, has only a weak influence on the jet height for untreated rafts, i.e. PE particles ($\rho_P = 1.35\,\mathrm{g\,cm^{-3}}$) and FPE particles ($\rho_P = 1.02\,\mathrm{g\,cm^{-3}}$) of comparable diameters reach similar jet heights, suggesting that particle inertia alone does not control the jet suppression.

A notable exception is seen for hydrophilic glass spheres (D_p = 625 μm), for which jetting occurs at $Fr \gtrsim 110$ (at a similar Fr number to that of much smaller PE particles). High-speed imaging shows that these glass particles submerge and are readily displaced downward upon impact, leaving a clear imprint of the crater on the pool surface. The particle coverage encountered by the collapsing cavity therefore quickly evolves, such that neither the initial packing fraction nor a static interparticle spacing can represent the raft geometry.

The particle mass transported by the jet scales approximately as $M_{\mathrm{p,jet}} \sim N_{\mathrm{jet}} \rho_p D_p^3$, where N_{jet} is the number of entrained particles. For the untreated (hydrophilic) glass raft, downward displacement of the particles reduces the number subsequently incorporated into the rising

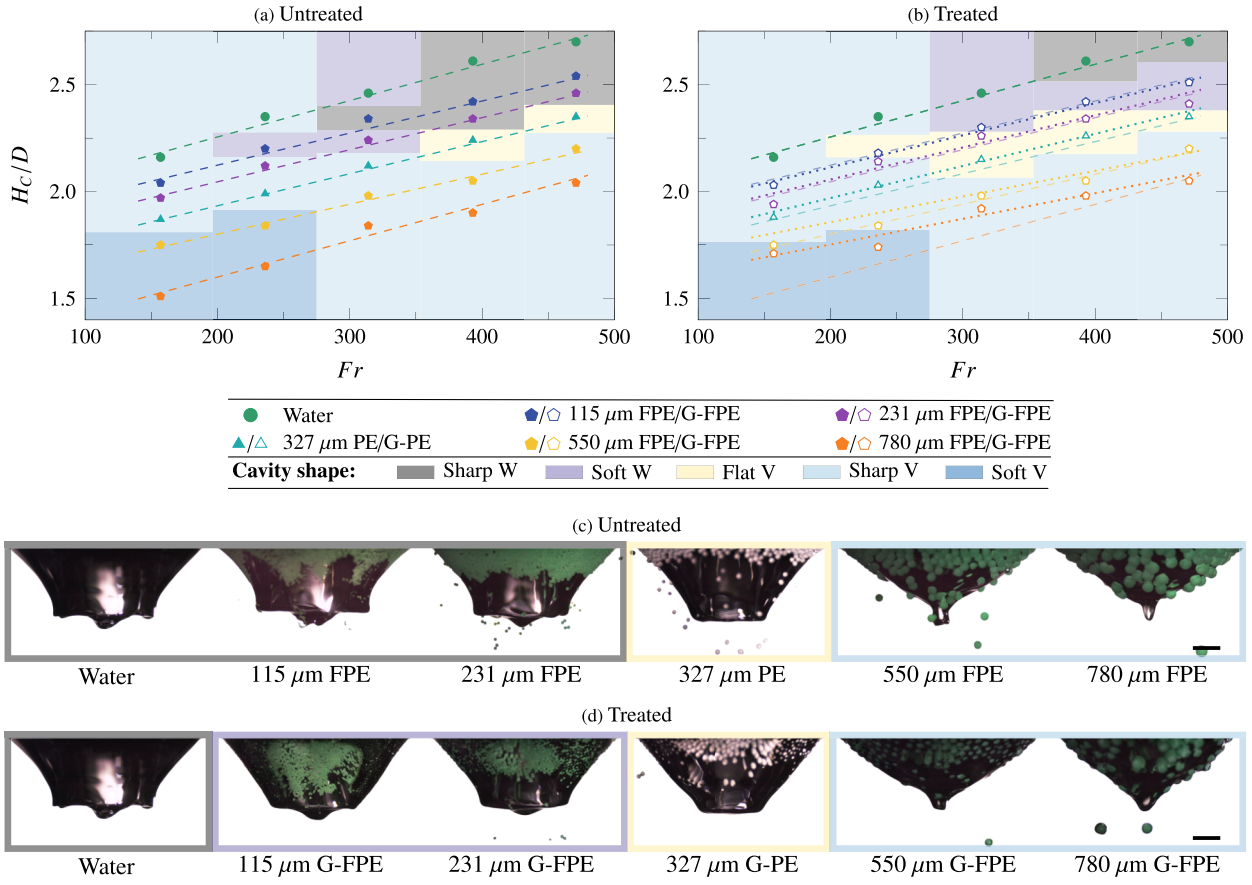


Fig. 5. Cavity depth and collapse morphology underlying jet formation on particle rafts. Solid symbols and dashed lines represent untreated particles, while hollow symbols and dotted lines represent Glaco-treated particles. a,b) Maximum dimensionless cavity depth, H_C/D, as a function of the Froude number Fr for clean water and particle rafts composed of FPE and PE particles of varying diameter. Untreated particles are shown in (a) and Glaco-treated seen in (b). For both conditions, cavity depth decreases monotonically with increasing particle size. In panel (b), dashed lines for untreated rafts are shown for reference. Shaded backgrounds denote the dominant cavity collapse shape identified from side-view imaging (legend). c,d) Representative side-view images of cavity collapse for untreated (c) and Glaco-treated (d) particle rafts at $Fr \approx 471$, illustrating the transition between sharp W, soft W, flat V and sharp V morphologies with increasing particle size and surface treatment. Shaded boundaries denote the dominant cavity collapse shape. Scale bars are 2 mm.

jet and therefore reduces the particle load that must be accelerated. Together with the locally depleted interfacial resistance encountered during cavity collapse, this partially restores the vertical momentum focusing required for jet formation despite the larger particle size and density.

A qualitatively different behavior emerges for Glaco-treated, superhydrophobic particle rafts (Fig. 4b). In all Glaco-treated cases, jet formation occurs at lower Froude numbers than for their size-matched untreated particles (except G-Glass), indicating early and efficient momentum focusing. For G-PE and G-FPE particle diameters of 115, 231 and 327 μm, jets appear at $Fr \gtrsim 70$, matching clean water. Larger Glaco-treated particles exhibit delayed jetting relative to smaller ones, but still at substantially lower thresholds than untreated rafts, with onsets at $Fr \gtrsim 110$ for 550 μm and $Fr \gtrsim 145$ for 780 μm. This indicates that, across Fr, superhydrophobic treatment makes the interface easier to mobilize and reorganize during collapse, thereby restoring earlier jet formation.

In contrast to untreated rafts, Glaco-treated surfaces show a non-monotonic variation of jet height with particle size. The tallest jets occur for intermediate diameters (231 and 327 μm), reaching heights comparable to, or marginally exceeding, those on clean water (Fig. 4d). Although smaller particles (115 μm) generate lower jets, their heights remain systematically higher than in the size-matched untreated case. A similar enhancement is observed for larger Glaco-treated particles (550 and 780 μm), which also produce taller jets than their untreated counterparts.

The sole exception to this behavior is provided by Glaco-treated (super-hydrophobic) glass spheres, for which jet formation is delayed to $Fr \gtrsim 145$ and the maximum jet height is markedly lower than for untreated glass. In contrast to the untreated (hydrophilic) particles, the superhydrophobic treatment prevents the dense glass spheres from submerging and promotes their entrainment into the rising jet. The corresponding increase in N_{jet}, combined with the large particle density and size, increases the particle load $M_{\text{p,jet}} \sim N_{\text{jet}} \rho_p D_p^3$ and limits the vertical growth of the jet. This also explains why particle density becomes more apparent once the big difference in immersion behavior is removed: although G-FPE and G-PE particles of different densities (1.02 and 1.35 g cm^{-3}, respectively) produce comparable jet heights at fixed particle size, the substantially denser G-Glass particles (2.50 g cm^{-3}) yield the lowest jets.

These results demonstrate that particle size, wettability, and inertia control jet formation and height, motivating a closer examination of the effect of upstream cavity formation and collapse dynamics on the jet behavior.

3.4. Cavity dynamics underlying jet formation

Our experiments demonstrate that regardless of the particle wettability, the Worthington cavity depth decreases monotonically with increasing particle size. Fig. 5a-b report the maximum cavity depth, H_C/D, measured relative to the undisturbed free surface, for both untreated and Glaco-treated particle rafts, respectively. As observed, on a clean water surface, the impact produces the deepest cavities across the explored Froude-number range. This indicates an efficient downward mo-

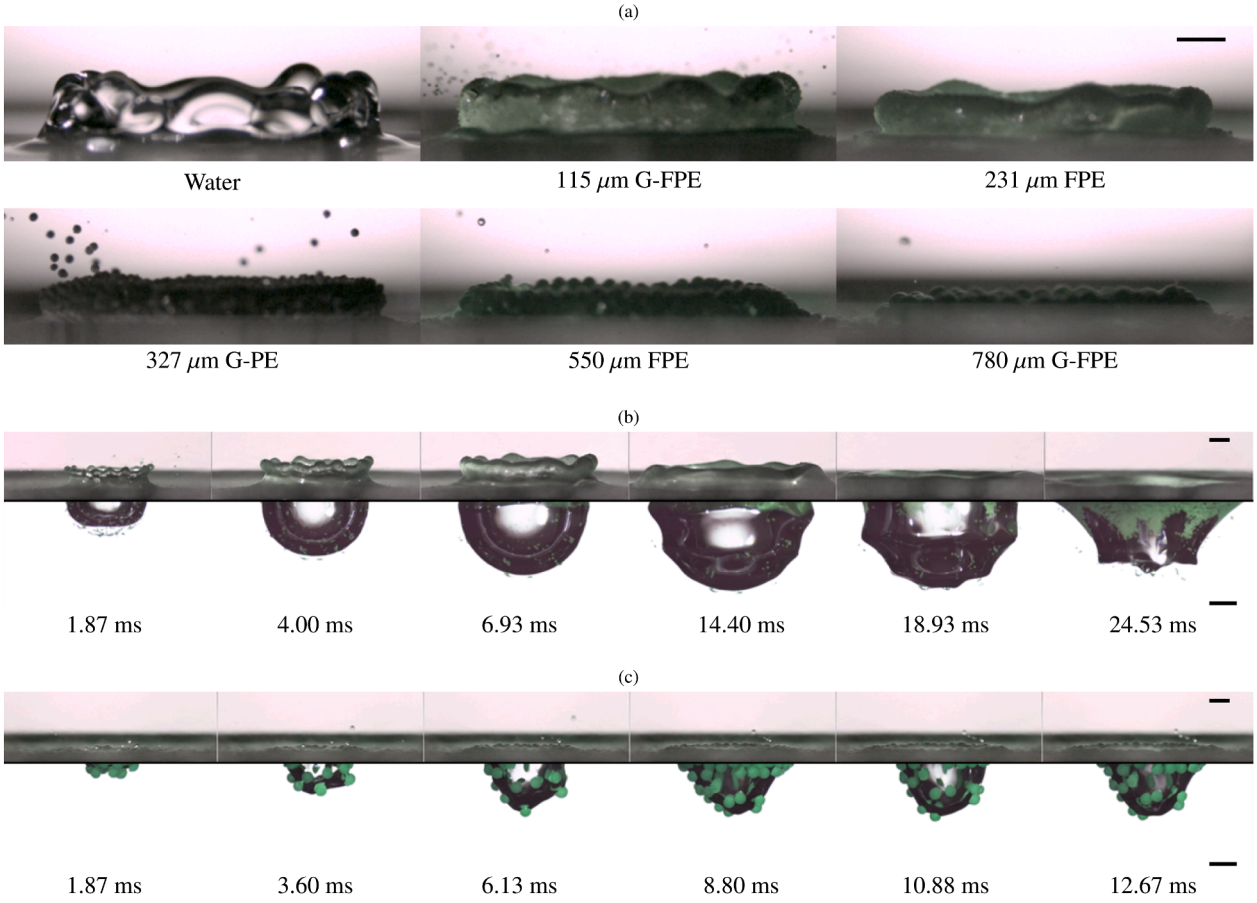


Fig. 6. Wave-swell development and suppression during cavity collapse on particle rafts. (a) Side-view snapshots at $t = 8.7$ ms after impact for clean water and rafts of increasing particle size at $Fr \approx 471$. The wave-swell magnitude decreases systematically with increasing particle size. **(b)** Synchronized, time-matched upper- and lower-view sequences for a representative sharp-W collapse on an untreated 115 μm FPE raft at $Fr = 471$. A pronounced wave swell develops and collapses inward, followed by a re-expansion of the cavity base. **(c)** Corresponding sequence for a representative soft-V collapse on an untreated 780 μm FPE raft at $Fr = 157$. The wave swell is substantially weaker and the cavity undergoes a simple closure without a pronounced base re-expansion. Times are measured from initial droplet contact. Scale bars are 2 mm.

mentum transfer and unobstructed cavity growth. Introducing a particle raft systematically reduces the cavity depth, with a clear decrease as particle size increases. Cavity depth decreases progressively from 115 to 780 μm particles, for both untreated and Glaco-treated rafts, indicating that larger particles increasingly impede cavity formation irrespective of surface treatment. Unlike the jet height, the cavity depth exhibits monotonic dependence on particle size for Glaco-treated rafts, with H_C/D decreasing with increasing particle diameter. We note that a systematic difference between treated and untreated rafts emerges as particle size increases (Fig. 5b). For the smallest particles (115 and 231 μm), the cavity depths for both rafts are nearly indistinguishable, indicating that surface treatment has little influence on the initial cavity penetration. However, this difference grows steadily with particle diameter: Glaco-treated rafts produce deeper cavities than their untreated counterparts for 327 μm particles, with the disparity becoming more pronounced for 550 and 780 μm particles. Taken together, these observations indicate that while deeper cavity formation explains the enhanced jetting on Glaco-treated rafts for large particles, it does not resolve the relatively stronger jet enhancement observed at smaller particle sizes. Consequently, the governing mechanism must instead lie in the cavity collapse. In the following section, we examine the cavity shapes and collapse dynamics in detail to establish how particle wettability and size control capillary-wave focusing and vertical momentum concentration during Worthington jet formation.

3.5. Cavity collapse modes

Fig. 5c-d present representative cavity shapes observed during collapse. The cavity shapes were classified visually from the side-view images. W-shaped cavities exhibit a central re-expansion during collapse, whereas V-shaped cavities converge towards a single central minimum. The descriptors “sharp” and “soft” qualitatively distinguish more localized, *pointy* profiles from broader, more rounded profiles, respectively. Fig. 6 additionally shows the evolution of the wave swell with particle size (a), together with time-resolved examples of representative sharp-W (b) and soft-V (c) collapse pathways.

As observed, on a clean water surface, the cavity dynamics following droplet impact exhibit a systematic progression with increasing Fr, governed by the interplay between the inertia of the collapsing wave swell and capillary retraction. This sequence follows established regimes for droplet impact on deep pools [30–32]. At high impact speeds ($Fr > 300$), a pronounced wave swell forms at the cavity rim, and its inward collapse generates a strong capillary-inertia wave that travels down the cavity wall. This wave induces a local re-expansion at the cavity floor, pinching it into a sharp W-shape. The subsequent collapse focuses momentum into a thick, slow Worthington jet that pinches off a single large droplet. At moderate Fr, the wave swell and the resulting capillary wave weaken. The cavity floor does not re-expand markedly, resulting in a soft W-shape or, at lower Fr, a sharp V-shape characteristic of a

more capillary-driven collapse. The retraction of these shapes produces a faster, thinner jet susceptible to capillary instabilities, which breaks into multiple smaller droplets. This morphological transition from a sharp W to a sharp V with decreasing Fr directly dictates the jet's morphology and the resulting droplet-size distribution [30–32].

The introduction of a particle raft fundamentally alters the cavity collapse sequence observed for a clean water surface. The raft's properties, particle size, and, critically, wettability, dictate whether the cavity follows a water-like collapse or a new, particle-mediated pathway. The particles control the efficiency of vertical momentum focusing and the characteristics of the ejected jet and droplets. For untreated particle rafts, the cavity morphology undergoes a systematic transition as particle size increases, shifting the collapse regime away from that of clean water. For the smallest particles (115 and 231 μm), the cavity shape at high Fr ($\gtrsim 300$) remains a sharp W, similar to clean water. Fig. 6 additionally shows the evolution of the wave swell with particle size (a), together with time-resolved examples of representative sharp-W (b) and soft-V (c) collapse pathways. This indicates that a pronounced wave swell is still able to form, consistent with the particle-size comparison in Fig. 6a. Its subsequent inward collapse and the associated re-expansion of the cavity base are shown directly in the time-resolved sequence in Fig. 6b. The resulting jet is consequently slow and thick, pinching off a single large droplet. However, as the particle size increases to 327 μm, this capacity is disrupted. The cavity at high Fr forms only a soft W (or a flat V), signaling a weakened wave swell. By 550 and 780 μm particle size, the cavity is exclusively sharp V-shaped even at the highest impact energies ($Fr = 471$). This morphological shift (from W to V with increasing particle size) demonstrates that larger, more massive rafts progressively suppress the formation and inward collapse of the wave swell, consistent with the systematic reduction in swell amplitude observed across particle sizes. The particle raft introduces additional pathways for energy redistribution and dissipation through particle rearrangement, interparticle interactions, contact-line motion, and interfacial deformation. These effects are distinct from bulk-liquid viscous dissipation and contribute to the suppression or redirection of wave-swell development and vertical momentum focusing. Consequently, the collapse mechanism transitions from the inertia-capillary wave-mediated process (sharp W) to a more direct, capillary-driven closure (sharp/soft V). A representative soft-V pathway is shown in Fig. 6c, where the weaker wave swell is followed by a simple cavity closure, without a pronounced base re-expansion. For the largest particles (550, 780 μm), the jet is slow and thick despite the cavity being a sharp V. This apparent contradiction is resolved by the role of particle entrainment. High-speed imaging confirms that these large particles are carried upward within the jet (Fig. 4c-d). This particle-laden jet is more stable against capillary breakup and remains uniform and thick, presenting a slower ascent and reduced height. The raft thus imposes a dual suppression: it first inhibits the W-forming collapse, and then the entrained particles dampen the jet dynamics.

Superhydrophobic treatment of the particle raft instigates a qualitatively different cavity evolution, characterized by the early ejection of particles and a consequent change in the energy partitioning during collapse. For small Glaco-treated particles (115 and 231 μm), the cavity at high Fr forms a soft W, distinct from the sharp W of clean water or untreated rafts of the same size. This is a pivotal observation: while cavity depth remains comparable to untreated cases, the shape is fundamentally different. The soft W and flat V indicate a diminished wave swell. Since the superhydrophobic coating enables immediate particle ejection during the initial splash and cavity opening, a significant portion of the impact energy is thereby diverted into the kinetic energy of scattered particles rather than into the potential energy of the wave swell. With a less massive and pronounced swell, the ensuing capillary-inertia wave is weaker, resulting in a softer re-expansion at the cavity floor (soft W or flat V versus sharp W). This altered collapse has profound consequences for the jet. The softer, less focused collapse does not produce the slow, thick Rayleigh jet. Instead, it facilitates a more efficient capillary retraction of the cavity walls, sparking a high-speed and thin jet. This explains the non-monotonic jet-height behavior: for the 231 μm Glaco-treated particles, the cavity depth remains broadly similar to that of the untreated case, while a clear transition from a sharper W-shaped cavity to a softer W-shaped cavity is associated with a taller, thinner jet. And for the 327 μm particles, both the untreated and Glaco-treated cases retain a broadly flat-V morphology. However, the Glaco-treated cavity is slightly shallower and more compact, with a smoother and more rounded base than the untreated case. This softening of the flat-V profile is consistent with more efficient vertical momentum focusing and the formation of a thinner, faster jet. As with untreated rafts, increasing the size of Glaco-treated particles eventually overwhelms this effect. For larger particles (550 and 780 μm), the cavity reverts to a sharp V at high Fr, and the jet becomes slower and thicker. The particle inertia is now too great for widespread early particle ejection; the raft behaves more rigidly, suppressing the wave swell entirely and returning to a V-shaped, capillary-driven collapse. In conclusion, the enhanced jet seen on intermediate-sized Glaco-treated particles is directly linked to the soft W cavity morphology and a direct consequence of wettability-driven particle ejection.

3.6. Jet height scaling and regime-dependent collapse

In this section, we seek a minimal scaling that captures both inertial momentum focusing and the resistance imposed by the particle raft. For a clean interface, the maximum dimensionless jet height follows a power-law dependence on Froude number, $h^* \propto Fr^{\alpha}$, describing its increase with impact inertia [30–32]. The subsequent Worthington jet results from capillary-driven cavity retraction and inertial momentum focusing. The presence of a particle monolayer reduces this focusing efficiency. We account for this additional resistance through a multiplicative attenuation factor $(1+\Pi)^{-1}$, yielding

$$h^* \propto \frac{\mathrm{Fr}^{\alpha}}{1+\Pi}, \qquad \Pi = \frac{D_p}{D}\frac{\rho_p}{\rho}(1+\cos\theta), \tag{2}$$

where Π quantifies the combined geometric, inertial, and wettability-dependent constraint imposed by the raft. Plotting $h^*(1+\Pi)$ against Fr on logarithmic axes (Fig. 7) reveals two approximately linear clusters with distinct slopes corresponding to two dynamical regimes of cavity collapse. Representative images illustrate the collapse dynamics associated with these regimes.

The distinction between the two dynamical responses is also supported by the established mechanics of closely packed particle rafts. Close-packed particle monolayers at liquid–air interfaces have been shown to behave collectively as two-dimensional elastic solids, supporting anisotropic stresses and exhibiting elastic buckling under compression [46]. Their resistance to out-of-plane curvature deformation can be characterized by a capillary bending stiffness, B [53]. For densely packed spherical particles,

$$B = \sigma D_p^2 \phi_s \left[\cos^2\theta \sin^2\theta + \frac{13}{24}\sin^4\theta\right],$$

where $\phi_s = \pi/(2\sqrt{3})$ corresponds to an ideal close-packed monolayer. Using the measured contact angles, the estimated B reported in Table 1 increases strongly with particle diameter. For untreated FPE, for example, B increases from approximately 0.47 nN m at $D_p = 115$ μm to 21.64 nN m at $D_p = 780$ μm.

The observed change between wave-swell-supporting and wave-swell-suppressed dynamics occurs around an approximate bending stiffness crossover of $B \sim 3$ nN m, with the boundary conditions spanning approximately 2.8–3.8 nN m. We therefore use "elastic" to describe the relatively low-B response, in which the raft remains sufficiently compliant to support pronounced wave-swell formation and collapse, and "rigid" to describe the relatively high-B response, in which curvature deformation and wave-swell development are strongly suppressed. These terms refer specifically to the collective elastic character and relative bending response of the particle raft.

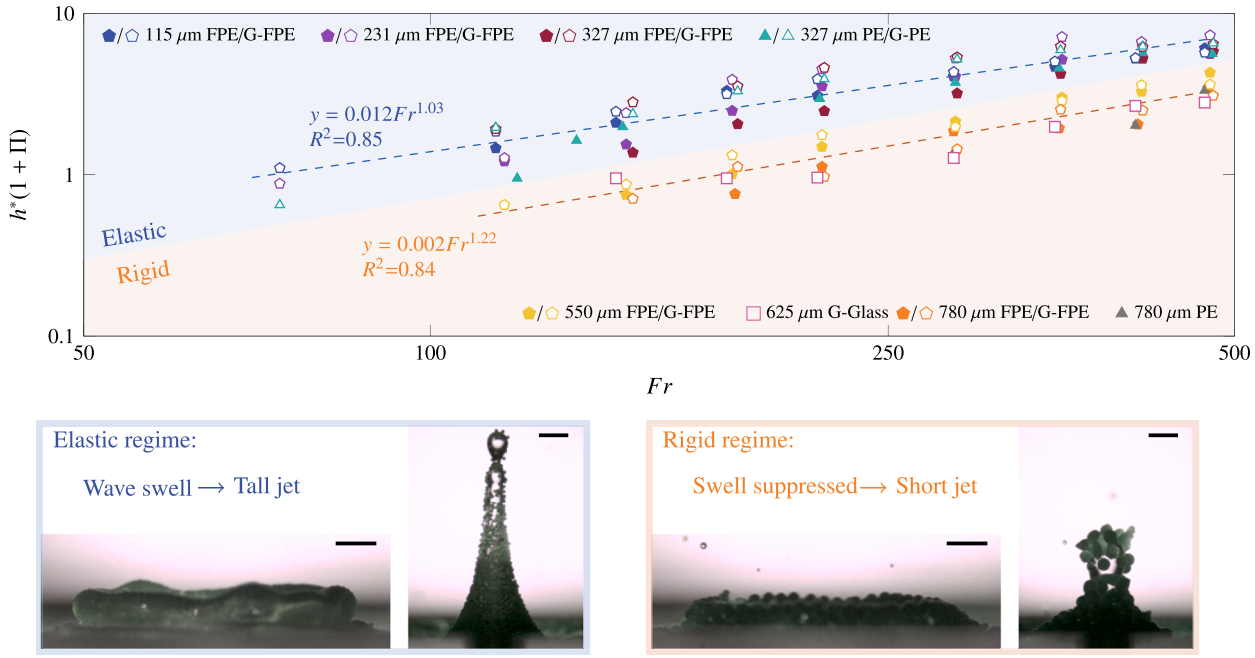


Fig. 7. Regime-dependent collapse of Worthington jet height. Collapsed representation of the dimensionless jet height $h^*(1+\Pi)$ as a function of Froude number for all particle types and surface treatments. The data separate into two distinct trends corresponding to elastically responsive (upper band, blue) and inertially rigid (lower band, orange) interfacial regimes. Dashed lines indicate power-law fits within each regime, highlighting the systematic difference in scaling behavior across particle sizes and densities. Representative side-view images below illustrate the collapse dynamics associated with these regimes: particle rafts in the elastic regime support wave-swell formation that promotes strong capillary-inertial focusing and tall jets, whereas in the rigid regime swell development is suppressed, resulting in weaker focusing and shorter jets. (For interpretation of the references to color in this figure legend, the reader is referred to the web version of this article.)

Hydrophilic glass particles form a special case: their large immersion depths lead to submergence and displacement from the interface during impact, preventing the formation of a persistent particle raft during collapse. Their dynamics therefore fall outside the present scaling and are excluded.

Within each regime, the data collapse onto a single power-law relation. In the elastic regime, the jet height scales nearly linearly with inertia, with $\alpha \approx 1.03$ ($R^2 \approx 0.85$). In the rigid regime, a steeper dependence is observed, $\alpha \approx 1.22$ ($R^2 \approx 0.84$), together with a prefactor lower than unity, indicating diminished vertical momentum focusing.

The separation between the regimes is consistent with the collapse mechanics identified earlier. When the raft remains sufficiently compliant, the wave swell can develop and collapse inward, promoting vertical momentum focusing. As the bending resistance increases, wave-swell development is suppressed and a greater fraction of the impact momentum is redistributed through particle motion and interfacial deformation, reducing the efficiency of jet formation. Despite the complexity of the interfacial dynamics, the jet height is therefore described by a minimal scaling in which inertial forcing is modulated by the geometric-inertial-capillary resistance of the particle raft.

3.7. Jet-mediated particle ejection and marble formation

Beyond impact-driven splashing, a second and often more consequential ejection pathway arises from the collapse of the impact cavity and the subsequent formation of a Worthington jet. Unlike particle splash, which is confined to the earliest stages of impact, jet-mediated ejection can transport particles vertically and generate airborne, particle-laden, droplets of sizes known for its environmental persistence (mist). The efficiency of this pathway is governed primarily by the cavity collapse morphology, which dictates jet velocity, thickness, and breakup behavior, and by particle-interface characteristics such as the immersion depth, inertia, and wettability. In brief, cavity collapse exhibits a transition from sharp V-shaped to sharp W-shaped morphologies as the Froude number increases for untreated rafts composed of small particles (115 – 327 μm). At high Fr, sharp W cavities produce a slow and thick jet that pinches off into a single, large tip droplet, often comparable in size to or larger than the original impacting drop. This droplet entrains a dense cluster of microparticles that is ejected vertically (Fig. 8a and Supplementary Movie 1). In this regime, jet-mediated ejection is dominated by the number of particles (~ 100) transported per droplet rather than by droplet count. At lower Fr, the same untreated rafts generate soft W, or sharp V, cavities, leading to fast thin singular jets. These jets undergo capillary breakup into multiple smaller droplets, each typically carrying only a few (~ 15 – 30) particles (Fig. 8b and Supplementary Movie 2). Although individual droplets transport fewer particles, the higher jet droplet count can result in a comparable or greater number of ejected particles. For small untreated rafts, at $Fr \approx 371$, jet breakup typically ejects ~ 50 particles per event (Fig. 8b). In contrast, impact-driven splash, i.e. $Fr \approx 471$, releases ~ 5 – 10 particles (Fig. 3a).

Superhydrophobic (Glaco-treated) rafts fundamentally transform the jet-mediated ejection pathway. For small treated particles, i.e. 115 – 327 μm, the cavity collapse takes the shape of a soft W, or a flat V, across the explored Fr range. This produces extremely fast and thin jets which, at early times, eject high-speed microdroplets that can transport significant particle loads into the air. As the jet develops, particles rapidly migrate and accumulate along the liquid-air interface, ultimately forming a continuous particle shell around the liquid column. This process gives rise to a fully armored, marble-forming jet (Fig. 8c and Supplementary Movie 3). There are two critical consequences of these dynamics: first, capillary breakup of the armored jet produces discrete droplets that remain fully coated, yielding stable liquid marbles that resist coalescence upon re-impact with the pool surface [54,55]. Second, the particle layer fundamentally alters the interfacial dynamics of the jet, enabling it to sustain high velocities while undergoing vigorous fragmentation. Together, these effects make the marble-forming jet a highly efficient ejection mechanism. It combines a high particle load per droplet with the production of numerous carrier droplets, thereby gener-

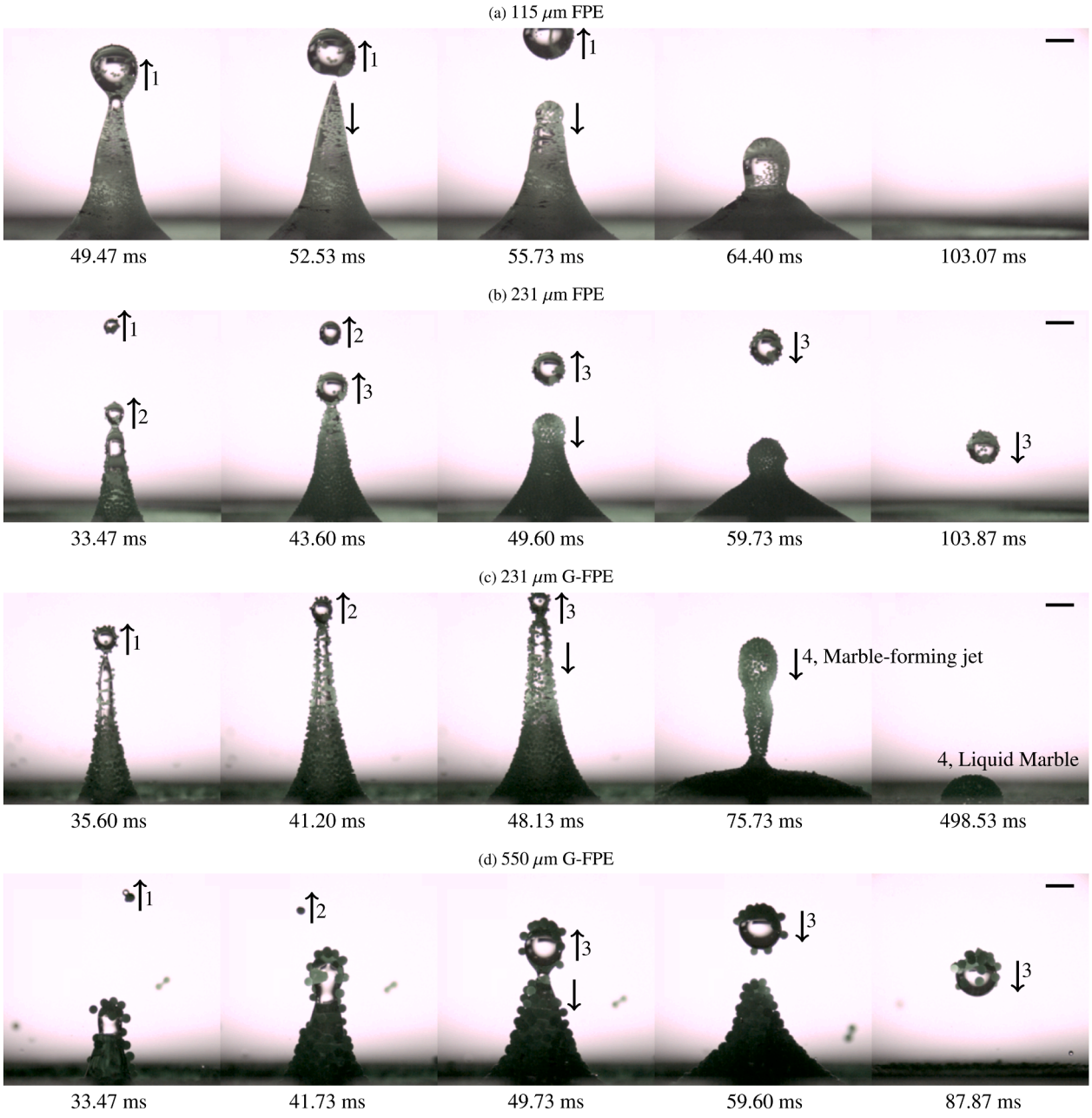


Fig. 8. Jet-mediated particle ejection and marble formation following cavity collapse. Time-sequence side-view snapshots showing representative modes of particle entrainment by the Worthington jet. Arrows indicate droplet trajectories, and time stamps denote elapsed time after impact. a) For 115 μm FPE untreated particles at $Fr \approx 471$, a sharp W-shaped cavity collapse produces a slow, thick cavity jet that pinches off a single large droplet carrying a compact cluster of microplastics. The droplet is rapidly ejected upward and leaves the field of view. b) For 231 μm FPE untreated particles at $Fr \approx 314$, a sharp V-shaped collapse generates a fast, thin jet that fragments into three smaller droplets via capillary instability, each transporting only a few particles. Two droplets are ejected at high speed and exit the frame, while the third decelerates and coalesces into the pool. c) For 231 μm G-FPE treated particles at $Fr \approx 471$, a soft W-shaped collapse produces an extremely fast and slender jet ejecting three fast tiny droplets that exit the frame. The jet becomes fully armored by particles, a marble-forming jet whose breakup yields a fourth larger, persistent liquid marble which remains intact upon returning to the interface. d) For 550 μm G-FPE treated particles at $Fr \approx 471$, a sharp V-shaped collapse produces a short, thick jet. Two individual particles are ejected upwards, and a single large droplet pinches off from the jet tip, carrying a small number of particles; this droplet decelerates and subsequently coalesces back into the pool. Supplementary Movies 1–4 present the complete time-resolved sequences corresponding to panels (a-d), highlighting the evolution of jet formation and particle entrainment.

ating a dense population of persistent airborne liquid marbles. Untreated hydrophobic PE and FPE rafts can also generate particle-laden droplets via the jet breakup; however, particle coverage in these cases remains partial rather than forming a continuous shell. These partially armored droplets lack the non-wetting shell characteristic of true liquid marbles and frequently coalesce upon falling back to the pool, limiting their atmospheric lifetime compared with the fully armored droplets produced by treated rafts.

For larger particles, i.e. $550 - 780\,\mu m$, jet-mediated ejection is strongly suppressed regardless of wettability. In this regime, cavity collapse is consistently forced towards a sharp V-shaped geometry across the explored Fr range, as the inertia of the raft suppresses wave swell

formation and vertical momentum focusing. Although the interface remains covered by particles, their large inertia inhibits jet acceleration and thinning. The resulting Worthington jet is short, thick, and flat, exhibiting weak vertical extension and limited breakup. Rather than fragmenting into multiple droplets, the jet produces at most a single, weak pinch-off event: a small number of individual particles may be accelerated upward, and a single particle-laden droplet can detach from the jet tip (Fig. 8d and Supplementary Movie 4). Consequently, jet-mediated ejection becomes inefficient as particle inertia dominates. The behavior of glass spheres provides a stringent confirmation of this hierarchy of governing parameters. Despite superhydrophobic treatment, their high density ($\rho_P \approx 2.50\,\mathrm{g\,cm^{-3}}$) prevents significant particle ejection during the jet phase. Their inertia imposes a severe load on the jet, suppressing jet height, thinning, and droplet formation, and thereby inhibiting aerosolisation through both impact- and jet-driven pathways.

Together, these results establish jet-mediated ejection as the dominant pathway for the atmospheric release of microplastics from particle rafts, particularly for small, weakly immersed, superhydrophobic particles. By directly linking cavity collapse morphology, jet dynamics, and particle armouring, this framework explains why such particles present the highest risk for long-range atmospheric transport via the formation of long-lived liquid marble aerosols.

4. Conclusion

Here, we have studied the impact of millimetric water droplets on liquid pools covered by floating microparticle rafts, revealing how particle size, density, wettability, and immersion depth govern splashing, cavity collapse, Worthington jet formation, and microplastic ejection. In contrast to previous studies that have considered ocean-to-atmosphere microplastic transfer through bubble bursting, sea-spray aerosol generation, or raindrop-driven surface entrainment [14,20–22,26], we show that a floating particle raft introduces an additional interfacial resistance that directly controls both early-time lamella dynamics and subsequent vertical particle transport. This links the physics of particle-laden liquid interfaces with classical droplet-impact and Worthington-jet dynamics [23,24,29–31].

Firstly, we have demonstrated that splash onset on particle rafts is not governed by a single material property, but by a combined geometric–inertial–capillary resistance. This behavior is captured by the scaling parameter $\Lambda = (D_p/D)(\rho_p/\rho)(1-\cos\theta)^3$, which collapses the spreading–splashing transition across particle materials, sizes, densities, and surface treatments. Small particles (115–327 μm) with substantial immersion depths stabilize the spreading lamella, delaying splash onset and limiting early ejection to small secondary droplets. In contrast, larger particles (550–780 μm), or weakly immersed superhydrophobic particles, protrude further above the interface and act as an effective rough particle layer. These rafts destabilize the lamella rim, promote fingering, and trigger splashing at lower Weber numbers, consistent with the known influence of lamella destabilization, surface roughness, and dynamic contact angle on splashing [25,51,52].

Secondly, we have shown that the particle raft controls not only splash onset but also the cavity-collapse pathway responsible for Worthington jet formation. On clean liquid pools, the collapse of the impact cavity focuses momentum into an upward jet whose morphology depends on the balance between inertia, capillarity, and gravity [29–33]. Here, the particle raft either redirects or suppresses this focusing depending on the particle properties. Small and intermediate rafts remain sufficiently compliant to support wave-swell formation and efficient vertical momentum focusing, whereas larger or denser rafts behave as inertially rigid layers that suppress wave-swell development and reduce the jet height. Despite these complex multiphase dynamics, the maximum jet height is described by $h^* \propto \mathrm{Fr}^{\alpha}/(1+\Pi)$, where $\Pi = (D_p/D)(\rho_p/\rho)(1+\cos\theta)$ represents the effective geometric–inertial resistance imposed by the raft. When rescaled by $(1+\Pi)$, the data separate into an elastically responsive regime, with near-inertial scaling ($\alpha \approx 1$), and an inertially rigid regime, where vertical momentum focusing is reduced.

Thirdly, we have identified two particle-transfer pathways from raft-covered interfaces. Impact-driven ejection occurs during the early lamella expansion and is favored by weakly immersed superhydrophobic particles, for which capillary adhesion to the interface is reduced. Jet-mediated ejection occurs later, during cavity collapse, and can transport particles vertically within the Worthington jet. Superhydrophobic rafts composed of small and intermediate particles produce particle-armored jets that fragment into liquid marbles, whereas untreated rafts generally form partially armored droplets that are more likely to coalesce upon returning to the pool. Since liquid marbles resist coalescence due to their particulate shell [54,55], this marble-forming pathway may provide an efficient route for producing persistent particle-laden droplets. These observations are also consistent with the broader behavior of particle rafts and armored droplets at liquid interfaces [37,42,43].

Together, these findings reveal how floating particulate monolayers transform canonical droplet-impact dynamics by coupling lamella destabilization, capillary adhesion, cavity-collapse morphology, and vertical jet formation. The proposed scaling arguments provide a predictive basis for identifying the interfacial conditions under which rainfall can transfer microplastics from water to air. More broadly, this work extends droplet-impact theory to particle-laden and contaminated interfaces, with relevance to sea-surface microlayers, environmental aerosolisation, soil erosion, sandy substrates, and other droplet–granular impact processes.

CRediT authorship contribution statement

Muhammad Hamza Iqbal: Writing – original draft, Visualization, Validation, Methodology, Investigation, Formal analysis, Data curation, Conceptualization; **Alfonso Arturo Castrejón-Pita:** Writing – review & editing, Resources, Funding acquisition; **José Rafael Castrejón-Pita:** Writing – review & editing, Supervision, Resources, Funding acquisition; **Miguel A. Quetzeri-Santiago:** Writing – review & editing, Supervision, Methodology, Investigation, Conceptualization.

Ethics declaration

The author(s) declare(s) that the study does not involve humans nor animal subjects.

Declaration of generative AI and AI-assisted technologies in the writing process

During the preparation of this work, the author(s) used Google Gemini for minor language suggestions and refinements. After using this tool/service, the authors reviewed and edited the content as needed and take full responsibility for the content of the publication.

Declaration of competing interest

The authors declare that they have no known competing financial interests or personal relationships that could have appeared to influence the work reported in this paper.

Acknowledgements

This work was supported by a UCL STEPS Grant (Project 586921). M.A.Q-S acknowledges support from DGAPA through Subprograma de Incorporación de Jóvenes Académicos de Carrera (SIJA) and the grant PAPIIT-UNAM IA101025; and support from the CIC through the Programa de Movilidad Académica Nacional e Internacional para el Subsistema de la Investigación Científica. A.A.C-P acknowledges support from

the Natural Environment Research Council grant UKRI1271 and the UK Engineering and Physical Sciences Research Council via Core Equipment Award UKRI424.

Data availability

Data will be made available on request.

Supplementary material

Supplementary material associated with this article can be found in the online version at 10.1016/j.patcog.2025.112367.

References

[1] J.R. Jambeck, R. Geyer, C. Wilcox, T.R. Siegler, M. Perryman, A. Andrady, R. Narayan, K.L. Law, Plastic waste inputs from land into the ocean, Science 347 (6223) (2015) 768–771.
[2] M. Strokal, P. Vriend, M.P. Bak, C. Kroeze, J. van Wijnen, T. van Emmerik, River export of macro-and microplastics to seas by sources worldwide, Nat. Commun. 14 (1) (2023) 4842.
[3] M. Eriksen, L.C.M. Lebreton, H.S. Carson, M. Thiel, C.J. Moore, J.C. Borerro, F. Galgani, P.G. Ryan, J. Reisser, Plastic pollution in the world's oceans: more than 5 trillion plastic pieces weighing over 250,000 tons afloat at sea, PloS One 9 (12) (2014) e111913.
[4] A. Cózar, F. Echevarría, J.I. González-Gordillo, X. Irigoien, B. Úbeda, S. Hernández-León, Á.T. Palma, S. Navarro, J. García-de Lomas, A. Ruiz, et al., Plastic debris in the open ocean, Proc. Natl. Acad. Sci. 111 (28) (2014) 10239–10244.
[5] K. Pabortsava, R.S. Lampitt, High concentrations of plastic hidden beneath the surface of the Atlantic ocean, Nat. Commun. 11 (1) (2020) 4073.
[6] N.B. Hartmann, T. Hüffer, R.C. Thompson, M. Hassellöv, A. Verschoor, A.E. Daugaard, S. Rist, T. Karlsson, N. Brennholt, M. Cole, et al., Are we speaking the same language? Recommendations for a definition and categorization framework for plastic debris, Environ. Sci. Technol. 53 (3) (2019) 1039–1047.
[7] J.P. Frias, R. Nash, Microplastics: finding a consensus on the definition, Mar. Pollut. Bull. 138 (2019) 145–147.
[8] S. Allen, D. Allen, F. Baladima, V.R. Phoenix, J.L. Thomas, G. Le Roux, J.E. Sonke, Evidence of free tropospheric and long-range transport of microplastic at Pic du Midi observatory, Nat. Commun. 12 (1) (2021) 7242.
[9] S. Allen, D. Allen, V.R. Phoenix, G. Le Roux, P. Durántez Jiménez, A. Simonneau, S. Binet, D. Galop, Atmospheric transport and deposition of microplastics in a remote mountain catchment, Nat. Geosci. 12 (5) (2019) 339–344.
[10] N. Evangeliou, H. Grythe, Z. Klimont, C. Heyes, S. Eckhardt, S. Lopez-Aparicio, A. Stohl, Atmospheric transport is a major pathway of microplastics to remote regions, Nat. Commun. 11 (1) (2020) 3381.
[11] L.F. Amato-Lourenço, R. Carvalho-Oliveira, G.R. Júnior, L. dos Santos Galvão, R.A. Ando, T. Mauad, Presence of airborne microplastics in human lung tissue, J. Hazard. Mater. 416 (2021) 126124.
[12] L.C. Jenner, J.M. Rotchell, R.T. Bennett, M. Cowen, V. Tentzeris, L.R. Sadofsky, Detection of microplastics in human lung tissue using μFTIR spectroscopy, Sci. Total Environ. 831 (2022) 154907.
[13] L. Qiu, W. Lu, C. Tu, X. Li, H. Zhang, S. Wang, M. Chen, X. Zheng, Z. Wang, M. Lin, et al., Evidence of microplastics in bronchoalveolar lavage fluid among never-smokers: a prospective case series, Environ. Sci. Technol. 57 (6) (2023) 2435–2444.
[14] S. Allen, D. Allen, K. Moss, G. Le Roux, V.R. Phoenix, J.E. Sonke, Examination of the ocean as a source for atmospheric microplastics, PloS One 15 (5) (2020) e0232746.
[15] Y.K. Song, S.H. Hong, M. Jang, J.-H. Kang, O.Y. Kwon, G.M. Han, W.J. Shim, Large accumulation of micro-sized synthetic polymer particles in the sea surface microlayer, Environ. Sci. Technol. 48 (16) (2014) 9014–9021.
[16] Z.T. Anderson, A.B. Cundy, I.W. Croudace, P.E. Warwick, O. Celis-Hernandez, J.L. Stead, A rapid method for assessing the accumulation of microplastics in the sea surface microlayer (SML) of estuarine systems, Sci. Rep. 8 (1) (2018) 9428.
[17] A.D. Gray, H. Wertz, R.R. Leads, J.E. Weinstein, Microplastic in two South Carolina estuaries: occurrence, distribution, and composition, Mar. Pollut. Bull. 128 (2018) 223–233.
[18] Y.K. Song, S.H. Hong, M. Jang, G.M. Han, W.J. Shim, Occurrence and distribution of microplastics in the sea surface microlayer in Jinhae Bay, South Korea, Arch. Environ. Contam. Toxicol. 69 (3) (2015) 279–287.
[19] J.M. Gove, J.L. Whitney, M.A. McManus, J. Lecky, F.C. Carvalho, J.M. Lynch, J. Li, P. Neubauer, K.A. Smith, J.E. Phipps, et al., Prey-size plastics are invading larval fish nurseries, Proc. Natl. Acad. Sci. 116 (48) (2019) 24143–24149.
[20] M. Masry, S. Rossignol, B.T. Roussel, D. Bourgogne, P.-O. Bussière, B. R'mili, P. Wong-Wah-Chung, Experimental evidence of plastic particles transfer at the water-air interface through bubble bursting, Environ. Pollut. 280 (2021) 116949.
[21] D.B. Shaw, Q. Li, J.K. Nunes, L. Deike, Ocean emission of microplastic, PNAS Nexus 2 (10) (2023) pgad296.
[22] L.M. Oehlschlägel, S. Schmid, M. Lehmann, S. Gekle, A. Held, Water–air transfer rates of microplastic particles through bubble bursting as a function of particle size, Microplastics Nanoplastics 4 (1) (2024) 1.
[23] A.L. Yarin, Drop impact dynamics: splashing, spreading, receding, bouncing…, Annu. Rev. Fluid Mech. 38 (1) (2006) 159–192.
[24] S.T. Thoroddsen, The ejecta sheet generated by the impact of a drop, J. Fluid Mech. 451 (2002) 373–381.
[25] G. Agbaglah, R.D. Deegan, Growth and instability of the liquid rim in the crown splash regime, J. Fluid Mech. 752 (2014) 485–496.
[26] M. Lehmann, L.M. Oehlschlägel, F.P. Häusl, A. Held, S. Gekle, Ejection of marine microplastics by raindrops: a computational and experimental study, Microplastics Nanoplastics 1 (1) (2021) 18.
[27] C. Motzkus, E. Géhin, F. Gensdarmes, Study of airborne particles produced by normal impact of millimetric droplets onto a liquid film, Exp. Fluids 45 (5) (2008) 797–812.
[28] C. Motzkus, F. Gensdarmes, E. Géhin, Study of the coalescence/splash threshold of droplet impact on liquid films and its relevance in assessing airborne particle release, J. Colloid Interface Sci. 362 (2) (2011) 540–552.
[29] A.M. Worthington, R.S. Cole, A Study of Splashes, Longmans, Green and Company, 1908.
[30] B. Ray, G. Biswas, A. Sharma, Regimes during liquid drop impact on a liquid pool, J. Fluid Mech. 768 (2015) 492–523.
[31] G.-J. Michon, C. Josserand, T. Séon, Jet dynamics post drop impact on a deep pool, Phys. Rev. Fluids 2 (2) (2017) 023601.
[32] S.K. Das, A. Dalal, M. Breuer, G. Biswas, Evolution of jets during drop impact on a deep liquid pool, Phys. Fluids 34 (2) (2022) 022110.
[33] E. Castillo-Orozco, A. Davanlou, P.K. Choudhury, R. Kumar, Droplet impact on deep liquid pools: Rayleigh jet to formation of secondary droplets, Phys. Rev. E 92 (5) (2015) 053022.
[34] A. Singh, P. Kumar, Droplet impact dynamics onto a deep liquid pool of wavy free surface, Phys. Fluids 34 (2) (2022) 022107.
[35] E. Esmaili, Z.-Y. Chen, A. Pandey, S. Kim, S. Lee, S. Jung, Corona splashing triggered by a loose monolayer of particles, Appl. Phys. Lett. 119 (17) (2021) 174103.
[36] S. Qian, H. Ye, D.Z. Zhu, J. Lin, K. Hu, J. Feng, Experimental study of liquid drop impact on granular medium: drop spreading/splashing and particle ejection, Water Res. 267 (2024) 122486.
[37] S. Protière, Particle rafts and armored droplets, Annu. Rev. Fluid Mech. 55 (1) (2023) 459–480.
[38] M.M. Nicolson, The interaction between floating particles, in: Mathematical Proceedings of the Cambridge Philosophical Society, vol. 45, Cambridge University Press, 1949, pp. 288–295.
[39] D. Stamou, C. Duschl, D. Johannsmann, Long-range attraction between colloidal spheres at the air-water interface: the consequence of an irregular meniscus, Phys. Rev. E 62 (4) (2000) 5263.
[40] P.A. Kralchevsky, K. Nagayama, Capillary interactions between particles bound to interfaces, liquid films and biomembranes, Adv. Colloid Interface Sci. 85 (2-3) (2000) 145–192.
[41] D. Vella, L. Mahadevan, The "cheerios effect", Am. J. Phys. 73 (9) (2005) 817–825.
[42] B.P. Binks, T.S. Horozov (Eds.), Colloidal Particles at Liquid Interfaces, Cambridge University Press, 2006.
[43] P. Kralchevsky, K. Nagayama, Particles at Fluid Interfaces and Membranes: Attachment of Colloid Particles and Proteins to Interfaces and Formation of Two-Dimensional Arrays, vol. 10 of *Studies in Interface Science*, Elsevier, 2001.
[44] B.P. Binks, T.S. Horozov, Colloidal Particles at Liquid Interfaces: An Introduction, Cambridge University Press, 2006, p. 1-74.
[45] L. Bergström, Structure and Formation of Particle Monolayers at Liquid Interfaces, Cambridge University Press, 2006, p. 77–107.
[46] D. Vella, P. Aussillous, L. Mahadevan, Elasticity of an interfacial particle raft, EPL 68 (2) (2004) 212–218.
[47] P. Cicuta, D. Vella, Granular character of particle rafts, Phys. Rev. Lett. 102 (13) (2009) 138302.
[48] P. Zuo, J. Liu, S. Li, The load-bearing ability of a particle raft under the transverse compression of a slender rod, Soft Matter 13 (12) (2017) 2315–2321.
[49] P. Zuo, J. Ji, R. Tadmor, J. Liu, Wrinkling number and force of a particle raft in compression, Eur. Phys. J. E 42 (11) (2019) 147.
[50] M.A. Quetzeri-Santiago, A.A. Castrejón-Pita, J.R. Castrejón-Pita, The effect of surface roughness on the contact line and splashing dynamics of impacting droplets, Sci. Rep. **9** (2019) 15030.
[51] M.H. Iqbal, M.A. Quetzeri-Santiago, A.A. Castrejón-Pita, J.R. Castrejón-Pita, Droplet impact onto textiles: wetting, spreading, and lamella-controlled splashing, J. Colloid Interface Sci. (2025) 139385.
[52] M.A. Quetzeri-Santiago, K. Yokoi, A.A. Castrejón-Pita, J.R. Castrejón-Pita, Role of the dynamic contact angle on splashing, Phys. Rev. Lett. 122 (22) (2019) 228001.
[53] C. Planchette, E. Lorenceau, A.-L. Biance, Surface wave on a particle raft, Soft Matter 8 (8) (2012) 2444–2451.
[54] P. Aussillous, D. Quéré, Liquid marbles, Nature 411 (6840) (2001) 924–927.
[55] P. Aussillous, D. Quéré, Properties of liquid marbles, Proc. R. Soc. A Math. Phys. Eng. Sci. 462 (2067) (2006) 973–999.